JGR Space Physics

RESEARCH ARTICLE
10.1029/2021JA029320

Key Points:

- Atomic oxygen in mesosphere and lower thermosphere (MLT) from Sounding of the Atmosphere using Broadband Emission Radiometry and whole atmosphere community climate model with thermosphere and ionosphere extension (WACCM-X) has a semiannual oscillation (SAO) with maxima at solstices and at summer mid-high latitudes, opposite to that of MSIS
- Global Ionosphere Thermosphere Model (GITM) reproduces the T-I SAO with equinoctial maxima using MSIS [O] at lower boundary and with solstitial maxima using WACCM-X [O]
- GITM does not change the SAO phase between MLT and upper thermosphere on a seasonal scale

Supporting Information:

Supporting Information may be found in the online version of this article.

Correspondence to:

G. Malhotra,
garimam@umich.edu

Citation:

Malhotra, G., Ridley, A. J., & Jones, M. Jr. (2022). Impacts of lower thermospheric atomic oxygen and dynamics on the thermospheric semiannual oscillation using GITM and WACCM-X. *Journal of Geophysical Research: Space Physics*, *127*, e2021JA029320. https://doi.org/10.1029/2021JA029320

Received 6 MAR 2021
Accepted 22 DEC 2021

Author Contributions:

Conceptualization: Garima Malhotra, Aaron J. Ridley, McArthur Jones
Data curation: Garima Malhotra
Formal analysis: Garima Malhotra, McArthur Jones
Funding acquisition: Aaron J. Ridley
Investigation: Garima Malhotra, McArthur Jones
Methodology: Garima Malhotra, Aaron J. Ridley

Impacts of Lower Thermospheric Atomic Oxygen and Dynamics on the Thermospheric Semiannual Oscillation Using GITM and WACCM-X

Garima Malhotra[1,2], Aaron J. Ridley[1], and McArthur Jones Jr.[3]

[1]Climate and Space Sciences and Engineering, University of Michigan, Ann Arbor, MI, USA, [2]CIRES, University of Colorado, Boulder, CO, USA, [3]Space Science Division, U.S. Naval Research Laboratory, Washington, DC, USA

Abstract The latitudinal and temporal variation of atomic oxygen (O) is opposite between the empirical model, NRLMSISE-00 (MSIS) and the whole atmosphere model, whole atmosphere community climate model with thermosphere and ionosphere extension (WACCM-X) at 97–100 km. Atomic Oxygen from WACCM-X has maxima at solstices and summer mid-high latitudes, similar to [O] from Sounding of the Atmosphere using Broadband Emission Radiometry (SABER). We use the densities and dynamics from WACCM-X to drive the Global Ionosphere Thermosphere Model (GITM) at its lower boundary and compare it with the MSIS driven GITM. We focus on the differences in the modeling of the thermospheric and ionospheric semiannual oscillation (T-I SAO). Our results reveal that driving GITM with WACCM-X causes the T-I SAO to maximize around solstices, opposite to when MSIS is used. This is because the global mixing in GITM during solstices is not strong enough to decrease the solstitial [O] densities below the equinoctial values between mesosphere and lower thermosphere (MLT) and upper thermosphere. Larger summer [O] in the MLT leads to the accumulation of [O] at lower latitudes in the thermosphere due to weaker meridional transport, which further increases the amplitude of the oppositely phased SAO. WACCM-X itself has the right phase of SAO in the upper thermosphere but wrong at lower altitudes. The exact mechanisms that can correct the phase of T-I SAO in GITM while using SABER-like [O] in the MLT are currently unknown and warrant further investigation. We suggest mechanisms that can reduce the solstitial maxima in the lower thermosphere, for example, stronger interhemispheric meridional winds, stronger residual circulation, seasonal variations in eddy diffusion, and momentum from breaking gravity waves.

Plain Language Summary We study the characteristics and drivers of the Thermospheric and Ionospheric Semiannual Oscillation (T-I SAO) using a numerical model of the Earth's upper atmosphere. It is an oscillation in T-I densities, temperature, and composition with maxima at equinoxes. We investigate the contribution of lower atmosphere to the T-I SAO using different assumptions at the lower boundary of the model. We find that using the correct lower boundary conditions changes the phase of T-I SAO such that it does not match with the satellite observations at higher altitudes. This implies that there are mechanisms missing in the numerical model that can reproduce the correct SAO phase while using the updated boundary conditions.

1. Introduction

The Earth's atmosphere is an open system with complex interplay between internal and external drivers resulting in complicated nonlinear coupling mechanisms. The region above 100 km is usually referred to as the Earth's upper atmosphere with the neutral thermosphere coexisting with the partly ionized ionosphere. Both the thermosphere and ionosphere exhibit several periodic variations in densities and temperature across an array of timescales ranging from minutes to a few years (Rishbeth, 2007). These include variations due to gravity waves (e.g., S. L. Bruinsma & Forbes, 2008; Miyoshi et al., 2014), tides (e.g., Forbes et al., 2009; Hagan et al., 2009), planetary waves (Sassi et al., 2016), annual and semiannual oscillation (e.g., Jones, Emmert, et al., 2018), quasi-biennial oscillation (e.g., Malhotra et al., 2016), and 11-year solar cycle (e.g., J. T. Emmert et al., 2008; Burns et al., 2015). Among the long-term variations, the thermospheric and ionospheric annual oscillation (T-I AO) and the semiannual oscillation (T-I SAO) have the largest magnitudes and were initially observed in neutral densities derived from satellite drag measurements by Paetzold and Zschörner (1961). The global T-I AO has a minimum in neutral densities in July and has partially been attributed to the changing distance between the Sun and the

Project Administration: Aaron J. Ridley
Resources: Garima Malhotra, Aaron J. Ridley
Software: Garima Malhotra, Aaron J. Ridley
Supervision: Aaron J. Ridley
Validation: Garima Malhotra, Aaron J. Ridley
Visualization: Garima Malhotra
Writing – original draft: Garima Malhotra
Writing – review & editing: Garima Malhotra, Aaron J. Ridley, McArthur Jones

Earth (Volland et al., 1972), and is still under investigation (e.g., Qian et al., 2009). In this study, we mainly focus on the T-I SAO. We will briefly review some of the pioneering works on T-I SAO in the following section.

1.1. Previous Work

The global T-I SAO has maxima in April and October and minima in January and July, and was initially hypothesized to be driven by the semiannual effect of geomagnetic activity (Paetzold & Zschörner, 1961). However, the SAO in geomagnetic activity itself was not well understood at the time (e.g., Bartels, 1932; Boller & Stolov, 1970). Among many theories, the Russell-McPherron (R-M) effect (C. T. Russell & McPherron, 1973) has been studied widely to explain the semiannual variation in geomagnetic activity. In this mechanism, during equinoxes, the magnetic field of the Sun in the ecliptic plane has larger southward magnitude on Earth in the Geocentric Solar Magnetospheric coordinates, resulting in stronger reconnection events. Walterscheid (1982) suggested that the semiannual variation in temperature (Joule Heating) due to the R-M effect is responsible for the globally averaged SAO in mass density. After Paetzold and Zschörner (1961), several other studies observed the SAO signature in O/N_2, atomic oxygen (O), temperature, and the ionospheric F2 layer (e.g., T. J. Fuller-Rowell, 1998; Jacchia et al., 1969; King-Hele, 1966; King-Hele, 1967; King-Hele & Kingston, 1968; Rishbeth & Mendillo, 2001; Rishbeth et al., 2000). The amplitude of the global T-I SAO has been recorded to be ∼15% in mass density at 400 km and ionospheric Total Electron Content (TEC) relative to the global annual average (J. Emmert, 2015; Jones et al., 2017). The T-I SAO was initially reproduced using temperature variations by the Jacchia series of thermospheric models (Jacchia, 1965, 1970). However, it was later observed that the temperature variations could not completely explain the SAO amplitude in thermospheric density and composition at solar minimum (G. Cook, 1967; G. E. Cook, 1969b; G. Cook & Scott, 1966). G. E. Cook (1969a) reported on the SAO in mass density at 90 km using rocket data and suggested that the source of T-I SAO is possibly in the mesosphere or the stratosphere. Jacchia (1971) and Jacchia (1977) later updated their thermospheric model such that the T-I SAO was considered as a density variation rather than purely a temperature variation.

An internal thermospheric mechanism called the "thermospheric spoon" (TSM) was proposed by T. J. Fuller-Rowell (1998) using the Coupled Thermosphere Ionosphere Model (CTIM; T. Fuller-Rowell et al., 1996). According to this mechanism, at solstices, due to the tilt of the Earth, the temperature gradient between the two hemispheres results in a global-scale, summer-to-winter interhemispheric circulation. It is also marked by upwelling in the summer and downwelling in the winter. This circulation acts as a large-eddy resulting in a much more mixed thermosphere and a smaller scale height during solstices. Jones, Emmert, et al. (2018) showed using controlled simulations of Thermosphere Ionosphere Mesosphere Electrodynamics General Circulation Model (TIME-GCM) that the magnitude of SAO reduces to 2% relative to the annual average when the tilt of the Earth is reduced to 0°, thus proving that the obliquity of the Earth is the largest factor for the SAO in the Earth's upper atmosphere.

The TSM also results in larger densities of lighter species, such as atomic oxygen and helium, in the winter hemisphere (Cageao & Kerr, 1984; T. J. Fuller-Rowell, 1998; Mayr & Volland, 1972; Mayr et al., 1978; Rishbeth & Müller-Wodarg, 1999) via vertical and horizontal transport. The lifetime of O increases to several months in the mesosphere and lower thermosphere (MLT). As a result, it becomes susceptible to dynamic effects above the MLT region (Brasseur & Solomon, 1984). Higher [O] in the winter has been observed at altitudes as low as 140 km (Grossmann et al., 2000). Sutton (2016) showed that the meridional transport of lighter species is linked with vertical upwelling and downwelling in the two hemispheres, along with horizontal divergence and identified these as the primary mechanisms for the accumulation of light species at high winter latitudes.

As stated above, the T-I system has many external drivers. One such driver is the lower atmosphere. Soon after its discovery in the upper thermosphere, the SAO was found in the lower thermosphere and near the mesopause (e.g., G. E. Cook, 1969a, 1969b; Groves, 1972; King-Hele & Kingston, 1968; King-Hele & Walker, 1969). Waves propagating up from the lower atmosphere can couple linearly and nonlinearly with the background atmosphere or with each other and significantly affect the T-I SAO (Newell, 1966; Volland et al., 1972). Eddy diffusion has historically been used in atmospheric models to parametrize the effects of subgrid-scale gravity wave mixing and breaking on the background densities, temperature and winds (Hodges, 1969). Qian et al. (2009) and Qian et al. (2013) using the Thermosphere Ionosphere Electrodynamics General Circulation Model (TIE-GCM) observed that the magnitude of SAO in neutral densities, composition, and peak electron density and height can be improved by introducing a seasonal variation in the global eddy diffusion parameter (K_{zz}; with no variation in

latitude, longitude, or solar time) at the lower boundary of the model, with a maxima during solstices (primary maximum during northern hemisphere summer) and minima during the equinoxes. A larger value of K_{zz} in the MLT during the solstices will result in higher concentration of molecular species and lower concentration of lighter species, thus, decreasing the O/N_2, mean scale height, and total density in the thermosphere. The amplitude of SAO in K_{zz} has been under investigation by G. Swenson et al. (2018) and G. R. Swenson et al. (2019). It has recently been realized that the K_{zz} by Qian et al. (2009) represents net cumulative coupling from the lower atmosphere (see Jones et al., 2017) as Salinas et al. (2016) found the amplitude of SAO in K_{zz} derived from SABER CO_2 to be much smaller.

In fact, Jones et al. (2017) pointed out that K_{zz} due to gravity waves may not be a primary driver for SAO in the lower thermosphere but may only affect the phase of SAO. Tidal dissipation from the lower thermosphere also affects the T-I SAO (Jones et al., 2017; Siskind et al., 2014). Jones et al. (2017) used TIME-GCM to analyze the contribution of different terms in the globally averaged O continuity equation. They found that the SAO in [O] is forced by a cumulative effect of the advective, tidal, and diffusive transport of O. O is the major species above 200 km, therefore, any long-term variations are directly manifested in neutral and ionospheric densities in the upper atmosphere. Jones, Emmert, et al. (2018) suggested that the upper mesospheric O chemistry might play an important role in the return branch of the thermospheric spoon circulation, but recently showed its effects to be negligible on the T-I SAO amplitude (Jones et al., 2021). Qian et al. (2017) and Qian and Yue (2017) showed that lower thermospheric winter-to-summer residual circulation can also affect the amount of upwelling and downwelling at higher latitudes, thereby affecting the T-I SAO.

1.2. Scope and Approach

First principle T-I models such as TIE-GCM (Richmond et al., 1992) and Global Ionosphere Thermosphere Model (GITM; Ridley et al., 2006) have been widely used to study the contribution of the lower atmosphere to T-I SAO (e.g., Qian et al., 2009; Qian et al., 2013; Salinas et al., 2016; Wu et al., 2017). This is because their lower boundaries are at roughly 95 km or slightly above, therefore providing an opportunity to study the effect of different (imposed) lower boundary assumptions. Another category of models is the whole atmosphere models, for example, Whole Atmosphere Model and Whole Atmosphere Community Climate Model with thermosphere and ionosphere extension (WACCM-X) that simulate the entire atmospheric column (i.e., ground-to-space) and thus include physical and chemical processes that T-I models do not have. These models are invaluable in understanding the coupling of lower atmospheric phenomena and the T-I system. The use of both types of models has the potential to significantly advance our understanding of the contribution of the lower atmosphere to the T-I system. The coupling of the lower atmosphere with a T-I model can be achieved through multiple mechanisms, for example, by specifying large-scale MLT winds, densities and temperatures at the lower boundary, by introducing variations in eddy diffusion parameter, and by including migrating and non-migrating tides (and other waves) in the state variables.

The motivation for this study is to better understand how the T-I SAO is controlled by the [O] and winds distribution in the MLT region. It is important because the variations due to dynamics in the lower thermosphere map to higher altitudes via diffusive equilibrium (Picone et al., 2013). This goal is achieved through the alteration of GITM's lower boundary, which is typically specified by the empirical model, Mass Spectrometer and Incoherent Scatter Radar Model (MSIS). However, there is a huge uncertainty regarding the dynamics, turbulence, and neutral densities near the lower boundary of GITM. This is because, the lower boundary of GITM is in the MLT at ~97 km, which lacks long-term, global observations. Therefore, in order to improve the SAO, we use the whole atmosphere model, WACCM-X as the lower boundary for GITM and compare the effect on the T-I SAO relative to MSIS driven GITM. There is evidence that since WACCM-X includes the physical mechanisms of the lower atmosphere, it best represents the MLT state and thus the thermosphere more accurately (Dunker et al., 2015; Huba & Liu, 2020; J. Liu et al., 2018; McDonald et al., 2015; Qian et al., 2018). The use of WACCM-X is also motivated by different spatial and temporal variations of [O] in the lower thermosphere between MSIS and WACCM-X. The opposite latitudinal distribution in MSIS as compared to SABER data and WACCM-X has been previously studied (Malhotra et al., 2020). At ~95–100 km, MSIS shows a winter maxima, whereas SABER and WACCM-X show summer maxima (Malhotra et al., 2020; J. P. Russell et al., 2004; Sheese et al., 2011; Smith et al., 2010). Moreover, the global mean of [O] within WACCM-X in the MLT is almost 180° out-of-phase with MSIS. We investigate the effects of these opposite latitudinal and temporal [O] variations on the T-I SAO. We

also study the effects of having no SAO at the lower boundary, and of constraining the dynamics in the lower thermosphere toward WACCM-X. Note that the long-term variability in the MLT states used in this study from MSIS and WACCM-X have both annual and semiannual components (as well as higher order harmonics), and thus, the forcing at the two solstices is asymmetrical. Therefore, the variability at higher T-I altitudes intrinsically includes the annual variation as well. Since, our focus in this study is on understanding the amplitude and phase of the semiannual component of the intra-annual variability, we will be primarily discussing and referring to the T-I SAO. The annual component, that is, the asymmetry between June and December solstices will be explicitly pointed out in the text and should not be confused with the semiannual component.

2. Methodology

2.1. Models

2.1.1. Global Ionosphere Thermosphere Model (GITM)

GITM is a physics based first principles model developed at the University of Michigan by Ridley et al. (2006) that self-consistently solves the Navier Stokes equations for neutral, ion, electron densities, dynamics, and temperatures in the T-I region, without assuming a hydrostatic equilibrium. It uses a three-dimensional spherical grid with longitude, latitude, and altitude as the coordinate system with the lower boundary in the MLT at ∼97 km and the upper boundary at ∼500–600 km. In its default mode, MSIS and Horizontal Wind Model (HWM) are used for initial and lower boundary conditions. The T-I state in GITM depends on the external drivers of the model, such as solar Extreme Ultraviolet (EUV) inputs, solar wind parameters, energetic electron precipitation, and high latitude electrical fields. It can couple with other empirical and physics based estimates for these inputs. In the configuration used in this study, GITM uses the Weimer model (Weimer, 2005) for high-latitude potential, Flare Irradiance Spectral Model (FISM) EUV model (Chamberlin et al., 2008) for estimates of solar irradiance at different wavelengths, and NOAA POES hemispheric power-driven model (T. J. Fuller-Rowell & Evans, 1987) for estimates of energetic particle precipitation. The version of HWM used in this study is HWM14 (Drob et al., 2015). The GITM simulations in this study have a resolution of 2° × 4° (latitude × longitude), and roughly a third of scale height in altitude.

2.1.2. Whole Atmosphere Community Climate Model With Thermosphere and Ionosphere Extension (WACCM-X)

WACCM-X is a whole atmosphere model that is built on top of the Whole Atmosphere Community Climate Model (WACCM) and covers the atmospheric region from the surface to the 500–700 km (H. Liu et al., 2010; H.-L. Liu et al., 2018). WACCM itself is built on top of the Community Atmosphere Model (Lin, 2004) and is a part of Community Earth System Model. WACCM-X uses a conventional spatial grid of latitude, longitude, and pressure. It includes self-consistent neutral dynamics, electrodynamics, F-region ion transport and solves for ion/electron temperatures. Gravity waves are parameterized from both orographic and non-orographic sources and thus can be used for studying the coupling of T-I system with both geomagnetic drivers and the lower atmosphere (H.-L. Liu et al., 2018). In this study, we use WACCM-X 2.0 in the Specified Dynamics (SD) configuration in our simulations and will refer to it simply as WACCM-X. In the SD configuration, temperature, winds, and surface pressure in the troposphere and stratosphere are specified from the Modern Era Retrospective Analysis for Research and Applications (MERRA) data set (Rienecker et al., 2011). The simulations used in this study have a horizontal resolution of 1.9° × 2.5° (latitude × longitude).

Here, we use hourly averaged WACCM-X output files. WACCM-X outputs the mixing ratios of different species on a geographic latitude/longitude grid and pressure levels with temperature, winds, and geopotential height. Total number density is derived from pressure and temperature using the ideal gas law. Vertical motion (ω) is output in the units of Pa/s and is converted to vertical wind, W in m/s as follows:

$$W = -\frac{\omega}{\rho g}, \tag{1}$$

where, ρ is the total mass density and g is the acceleration due to gravity (assumed constant with altitude). Since GITM uses an altitude grid, the logarithm of the WACCM-X total number density is linearly interpolated to an intermediate altitude grid. This intermediate altitude grid is uniformly defined from 95 to 152.5 km. Other parameters such as mixing ratios, temperature, and winds are linearly interpolated onto this altitude grid. The

Table 1
GITM Runs

Simulation	Density lower boundary condition	Winds lower boundary condition
G/MSIS	MSIS	HWM
G/NOSAO	MSIS with AO and SAO set to 0	0
G/WX	WACCM-X	WACCM-X
G/NUDGE	WACCM-X	Nudged to WACCM-X till 140 km

mixing ratios and total number densities are then multiplied to output the number density for each species on this new grid. The WACCM-X outputs on the altitude grid are then used in GITM, the specifications of which differ between different simulations used in this study. Further details of these simulations are discussed in Section 2.2.

2.1.3. Mass Spectrometer and Incoherent Scatter Radar Model

The MSIS-class models (Hedin, 1983, 1987, 1991; Hedin et al., 1977) are empirical models of composition, temperature, and neutral density of Earth's atmosphere, derived from ground, rocket, and satellite-based measurements. MSISE-86 covers the altitude region from 90 km to the exobase, while MSISE-90 has the lower boundary at the surface. These models were a significant improvement over the Jacchia-class models, which were also empirical models that estimated total mass density from orbital decay of objects that flew from 1961 to 1970 (Jacchia, 1965, 1970, 1971). NRLMSISE-00 (Picone et al., 2002) also extends from the ground to the exobase and includes additional data spanning 1965–1983 from the Jacchia models. This includes data from satellite accelerometers, incoherent scatter radars, mass spectrometers, solar ultraviolet occultation, and drag measurements up to the mid-to-late 1990s. It also contains more data covering high latitudes and extreme cases of geomagnetic forcing. In this study, we use NRLMSISE-00 for the lower boundary condition in GITM. A new, improved NRLMSIS 2.0 model (J. T. Emmert et al., 2020) that ingests SABER [O] measurements has recently been released, and represents MLT [O] much better. At the time of writing this manuscript, all the simulations were already completed with the NRLMSISE-00. We do plan to change the lower boundary in GITM to NRLMSIS 2.0 in the future. In this manuscript, we will refer to NRLMSISE-00 simply as MSIS.

2.2. GITM Simulations

The GITM simulations used in this study are for 2010 and use measured time-varying geospace indices to specify high-latitude and solar EUV drivers so that the results can be validated against observational data sets. This year was chosen because it was a geomagnetically quiet year during a solar minimum, which emphasizes the lower atmospheric effects on the upper thermosphere. The lower boundary of GITM is controlled by two ghost cells in altitude below 100 km, which are filled with densities, temperatures, and winds. These are then used in the solvers for the first couple of lower cells in GITM, so that they control the dynamics in these cells. Table 1 summarizes these simulations. All these simulations use a K_{zz} value of 300 m^2/s that is constant with time.

The default configuration is the G/MSIS simulation. In this configuration, for neutral densities, only the second ghost cell nearest to 100 km is specified from MSIS. For the first cell, a hydrostatic solution for most neutral densities is projected from the second cell so as to not drive constant nonzero acceleration. [O] and T are specified from MSIS and kept the same in both the cells. Horizontal winds are specified by HWM in the second cell and determined in the first cell similar to densities using the gradients from cells above. Since, HWM only has horizontal winds, the vertical velocity for all species is determined in both the cells so as to have zero flux through the lower boundary, that is, the value in the first (second) ghost cell is the opposite of the value in the second (first) real cell. In the second simulation, G/NOSAO, we use GITM in its default configuration, but MSIS has the AO and SAO flags turned off for both symmetrical and asymmetrical components. The horizontal winds in the second cell are zero. In the first cell, they are nonzero and determined as discussed above.

In the third simulation, G/WX, we use WACCM-X as the lower boundary condition. For densities, similar to the default configuration, values are specified in the second cell only and hydrostatic condition is enforced in the first cell. [O] is the same in both the cells. However, for winds (including the vertical winds) and temperatures, values

are specified in both the cells from WACCM-X. Thus, there is a vertical flux of winds and temperature in this simulation, resembling more realistic atmospheric conditions.

In the fourth simulation, G/NUDGE, the lower boundary conditions are identical to the G/WX simulation, but from 100 to 140 km, GITM winds (full dynamical fields) are nudged toward WACCM-X winds. The vertical weighting function (ζ) for the nudging is similar to that used by Maute et al. (2015) and is as follows:

$$\zeta = \cos^2\left[\frac{\pi}{2}\left(\frac{z - z_{lb}}{z_{\max} - z_{lb}}\right)\right], \tag{2}$$

where, z_{lb} and $z_{\max}$ are 100 and 140 km, respectively. The nudging technique is similar to that used by Wang et al. (2017):

$$X(\lambda, \theta, z, t) = (1 - \alpha\zeta(z))X_G(\lambda, \theta, z, t) + \alpha\zeta(z)X_W(\lambda, \theta, z, t), \tag{3}$$

where, X represents zonal wind, meridional wind, and vertical wind fields. X_G and X_W represent the model fields from GITM and WACCM-X, respectively. In this technique, the GITM fields are constrained by the dynamics fields of Equation 3. The use of vertical profile implies that nudging is the strongest at 100 km and weakest at 140 km. This allows for a smooth transition from WACCM-X lower thermospheric dynamics to GITM dynamics in this simulation. α represents the relaxation factor and was discussed in detail by Jones, Drob, et al. (2018), and is defined as -

$$\alpha = G\Delta t, \tag{4}$$

where, G represents the inverse of relaxation time. $\alpha = 1$, implies that GITM fields are overwritten at every model time-step. Here, we use a relaxation time of 60s. The model time-step, Δt in GITM varies and is on average ~2s. This implies α would on average have a value of ~0.03.

2.3. Data Sets

We use a number of different data sets to validate the phase and amplitude of T-I SAO produced by the different simulations.

2.3.1. Sounding of the Atmosphere Using Broadband Emission Radiometry (SABER)

SABER is an instrument on NASA's Thermosphere Ionosphere Mesosphere Energetics Dynamics (TIMED) satellite. SABER provides global vertical profiles of temperature, pressure, geopotential height, volume mixing ratios, volume emission rates, and cooling and heating rates for several trace species in the MLT region (Mlynczak, 1996; Mlynczak, 1997; Russell et al., 1999; Yee, 2003). The version of the data set used in this study is V2.0 (Panka et al., 2018). We use 10-year averaged [O] data to understand its temporal and spatial distribution at 97 km. Averages for each year are derived by binning the data into a day of the year and latitude grid. Then, 10 years of data are averaged together.

2.3.2. Global Ultra-Violet Imager (GUVI)

GUVI is a UV spectrograph with primary objectives of measuring thermospheric composition, temperature, and high-latitude particle precipitation (Christensen et al., 2003; Paxton et al., 1999; Yee, 2003). In this study, we use the height-integrated O/N_2 derived from GUVI measurements. Integrated O/N_2 is defined as the ratio of integrated O to N_2 column densities, from the top of the atmosphere as defined by a model or the altitude of the satellite, downward until the altitude where the N_2 column integrated density reaches 10^{21} m^{-2} (Strickland et al., 1995). We will henceforth refer to it simply as O/N_2. In this study, we use the global average for 2010. It is derived by binning the data into a day of the year and latitude grid. We use the level 3 GUVI data product.

2.3.3. TIMED Doppler Interferometer (TIDI)

TIDI is a Fabry-Perot interferometer that measures global horizontal winds in the MLT region (Yee, 2003). In this study, we use TIDI data for 2010 to validate the meridional winds in the lower thermosphere. A 60-day average is determined after binning the data into an altitude and latitude grid. Level 3 vector data are used here.

2.3.4. Global Navigation Satellite System (GNSS)

GNSS data are used to determine the line-integrated ionospheric electron density by measuring the propagation time difference between two different radio frequencies (Vierinen et al., 2016). The measurements are scaled by 10^{16}m^{-2}, also referred to as total electron content (TEC) units. This slant ionospheric TEC is converted into vertical total electron content by using a scaling factor proportional to the elevation angle of the satellite from the receiver (Vierinen et al., 2016). The data that we use here have a spatial resolution of $1° \times 1°$ and a temporal resolution of 30 min. In this study, we use the global mean TEC for 2010 for the validation of the ionospheric SAO. It is derived by binning the data into a day of the year and latitude grid.

2.3.5. Challenging Minisatellite Payload (CHAMP) and Gravity Recovery and Climate Experiment (GRACE)

CHAMP and GRACE are low-earth orbit satellites with a primary objective of making accurate measurements of Earth's gravity field (Reigber et al., 2002; Tapley et al., 2004). They have highly accurate accelerometers that have been widely used to derive neutral density measurements from atmospheric drag measurements (e.g., S. Bruinsma et al., 2004; Lühr et al., 2004; Sutton, 2011). In this study, we use neutral mass density data sets from 2007 to 2010 from these satellites to validate the mass density SAO in the upper thermosphere. Averages for each year were derived by binning the data into a day of year and latitude grid.

2.3.6. Emmert Data Set

J. T. Emmert (2015) studied the trends in globally averaged neutral mass density from 1967 to 2013. This data set is derived from the orbits of ∼5,000 objects between the altitudes of 200 and 600 km (J. T. Emmert, 2009). These data have a resolution of 3–6 days with daily relative accuracy of ∼2% and absolute accuracy of 10%. In this study, we use the derived density data for 2010 at 400 km. We will henceforth refer to this data set simply as "Emmert ρ" or "Emmert data set."

3. Results

3.1. Motivation

Figure 1 shows the normalized integrated O/N_2, integrated vertical TEC, and mass density (ρ) for G/NOSAO and G/MSIS simulations, compared with different observational data sets and empirical models for 2010. The thin lines are the daily averages for all data and the thicker lines indicate fitted values. The fitted curves are derived by fitting a least squares annual and semiannual variation to the data. The red vertical lines indicate the solstices and equinoxes. All the values are normalized as specified below,

$$v_{\text{norm}} = \frac{v - \overline{v}}{\overline{v}} \times 100, \tag{5}$$

where, $\overline{v}$ represents the global annual average of value, v (where, v is ρ, TEC or O/N_2). In Figure 1a, an SAO with equinoctial maxima and an amplitude of 18% (with respect to its annual average) is observed in the GUVI O/N_2 data. The amplitude of SAO for different data is determined by fitting a semiannual variation. Since, O/N_2 is an integrated value, it largely reflects the lower T-I state at ∼140 km, as the densities decrease exponentially with altitude (Yu et al., 2020). G/NOSAO shows smaller SAO amplitude as compared to G/MSIS, which is in better agreement with the GUVI data and pure MSIS, thus demonstrating the importance of appropriate lower boundary SAO. The amplitude of SAO for GUVI is larger than that of MSIS. We can also compare the SAO phase of different simulations by analyzing their day of maxima and minima. The phase of both the simulations agrees well with the observations.

Figure 1b shows TEC for the two simulations compared with GNSS data. TEC being an integrated quantity has the largest contribution from the peak electron density altitude at ∼250–300 km. The SAO amplitude in GNSS TEC data is ∼13%, which is consistent with the climatological value calculated by J. T. Emmert et al. (2014). This is much less than that observed in GUVI O/N_2. Similar to Figure 1a, using MSIS as the lower boundary increases the SAO amplitude in GITM. There is also a small phase difference between the simulations and the

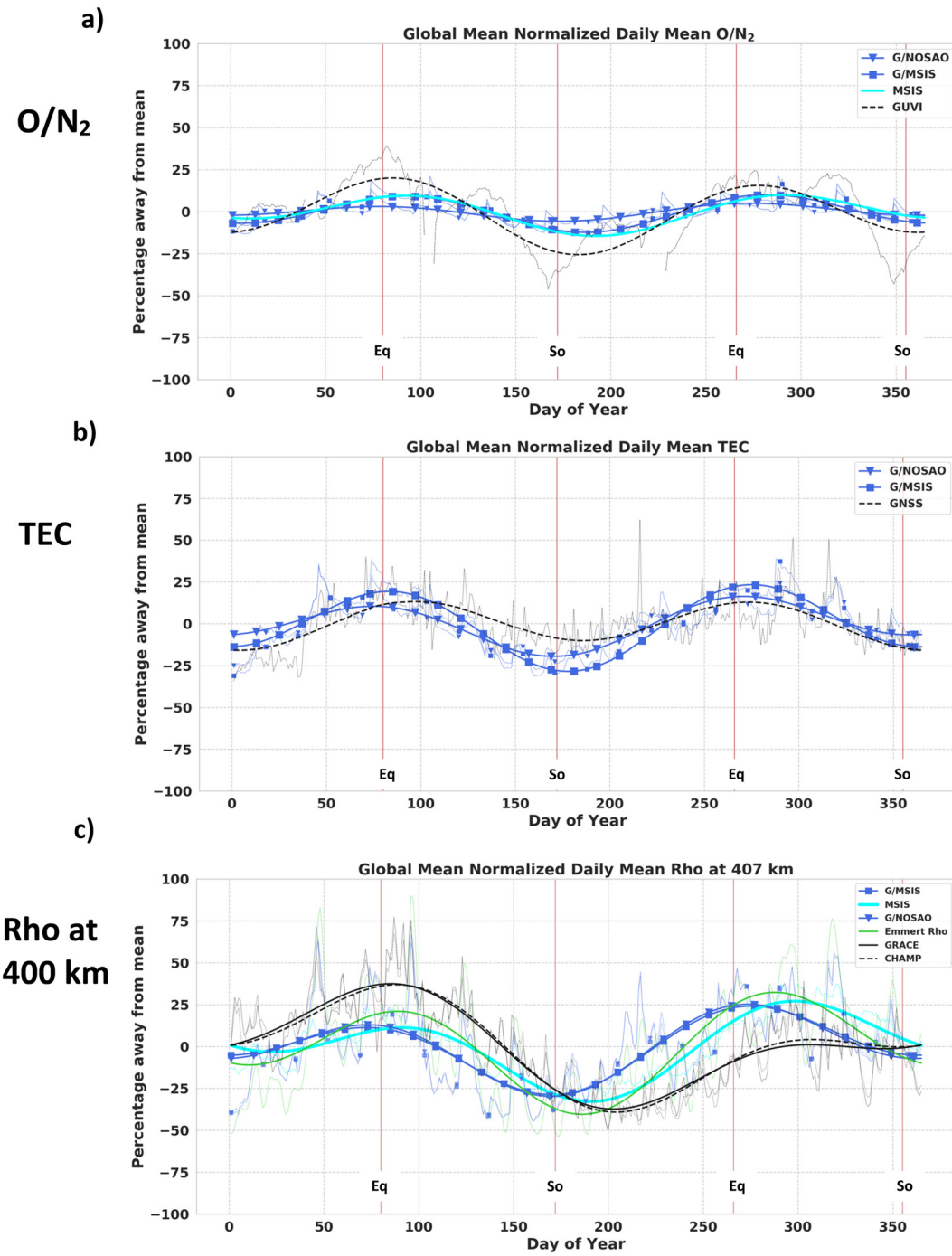

Figure 1. Diurnally Averaged Normalized (a) O/N_2, (b) Total Electron Content, and (c) ρ at 400 km, for Global Ionosphere Thermosphere Model simulations, MSIS and observational data sets. Challenging Minisatellite Payload and Gravity Recovery and Climate Experiment data sets are normalized to 400 km and averaged for 2007–2010 because of data gaps in 2010. The thin lines indicate the raw data and the thicker lines indicate the fitted values. The red vertical lines indicate the days of equinoxes (day 80 and day 266) and solstices (day 172 and 355).

GPS data, with GITM leading (peak earlier in the year) the data during March and June. G/MSIS lags behind the G/NOSAO, and is in better agreement with the phase of GNSS data.

Figure 1c shows the mass densities at ~400 km for both the simulations compared with those from the CHAMP and GRACE satellites (normalized at 400 km). The densities for CHAMP and GRACE are averaged between

2007 and 2010 because of data gaps in 2010. We also show values from the Emmert data set and the MSIS empirical model. In this altitude region, G/NOSAO and G/MSIS show agreement in both the SAO phase and amplitude. CHAMP and GRACE mass densities also agree well with each other. The largest disagreement is in the phase of the SAO. Both the model simulations lead the observations and empirical model, especially during June and September. Comparing with the Emmert data, GITM simulations have smaller deviations from the mean. An equinoctial asymmetry is also prominent in ρ and not as much in O/N_2 and TEC. MSIS, Emmert data, and GITM simulations have larger (smaller) densities during September (March) equinox, whereas CHAMP and GRACE have smaller (larger) values during this time. A similar observation was made by Lei et al. (2012) in the CHAMP and GRACE data, namely that the densities are larger during March than those around September during periods of high and moderate solar activity. Since CHAMP and GRACE data are averaged for 2007–2010, it is possible it does not accurately represent the thermospheric state during a geomagnetic quiet time (2010 for our purposes).

Note the phase of GUVI and GNSS data leads the CHAMP data, indicating that there is a phase progression in the T-I SAO with altitude that GITM is unable to capture. For example, GUVI and GPS data show a September maxima closer to equinox (day 266), whereas, the September maximum for CHAMP ρ is around day 280–300. Moreover, the phase progression with altitude is not uniform for different times of the year and is more prominent during June and September. This is different from the inference by Yue et al. (2019) as they observed that the phase of the SAO in height-resolved O/N_2 stays the same between the lower and upper thermosphere. An annual asymmetry is also quite noticeable for all the parameters shown in Figure 1. Lower O/N_2, TEC, and ρ are observed near June solstice as compared to the December solstice. Another interesting observation is that G/MSIS (the simulation in better agreement with the observational data sets), has smaller SAO amplitude than GUVI O/N_2 and Emmert ρ data set, but larger than GNSS TEC. The phase difference between the simulated SAO in G/MSIS and observational data sets is much larger for ρ, and smaller for O/N_2, and TEC. This observation delineates the challenge of the model-data comparison studies, and a possible reason might be inherent biases and uncertainties in different satellite data sets.

These results reveal that GITM is able to reproduce SAO in some of the T-I parameters, TEC, and ρ at 400 km without necessarily having an SAO at the lower boundary, but with lower amplitude and shifted phase. However, the SAO in composition, O/N_2 is much smaller, but not absent. This is not necessarily the case with other T-I models whose lower boundaries are between 95 and 100 km (e.g., TIE-GCM see Qian et al. (2009) and Jones et al., 2021). In the absence of a composition or eddy diffusion SAO imposed at the model lower boundary, the only major driver of the SAO is the thermospheric spoon mechanism. The SAO in TEC and ρ is also influenced by factors other than composition such as the transport, plasma scale height for TEC, and temperature for ρ. To eliminate the disagreements in the SAO amplitude and phase, the contribution from the lower atmosphere cannot be ignored. In the next section, we discuss the distribution of [O] in the MLT.

3.2. Lower Boundary Conditions

Figures 2a and 2b show 10-year averaged O number density from SABER at 85 and 97 km, while Figures 2c and 2d show the area-weighted global averages at each altitude. The global averages are only for the latitude region spanning $\pm 55^\circ$ because of missing data at high latitudes. Using a longer term average for satellite data reduces biases due to incomplete longitudinal sampling, tidal phases, missing data, etc., thus increasing the statistical significance.

The latitudinal distribution of [O] reverses between the two altitudes, consistent with what Smith et al. (2010) showed using an earlier version of the SABER [O] data. At 85 km, the higher latitudes show an annual variation with larger [O] during winter. This is because of the gravity wave induced summer-to-winter meridional circulation in the mesosphere and downwelling in winter (e.g., Garcia & Solomon, 1985; Holton, 1983; Lindzen, 1981). The lower latitudes show an SAO with maxima around the equinoxes, which is similar to the mesospheric semi-annual oscillation in zonal winds in the equatorial mesosphere (Garcia et al., 1997). The SAO in zonal winds has been found to be driven by momentum deposition by gravity waves that are selectively filtered by the stratospheric winds (Burrage et al., 1996). However, the mechanism for the SAO at 85 km in [O] is still under investigation. The lifetime of O in this altitude region is too short to be affected by a wind circulation of such a long period. Smith et al. (2010) suggested that the seasonal variation in the amplitude of the migrating diurnal tide might be a more likely source. It was demonstrated by Jones et al. (2014) that tides induce a net increase in [O] during equinoxes close to the equator via tidally induced advective transport. Figure 2c shows that at 85 km, the global

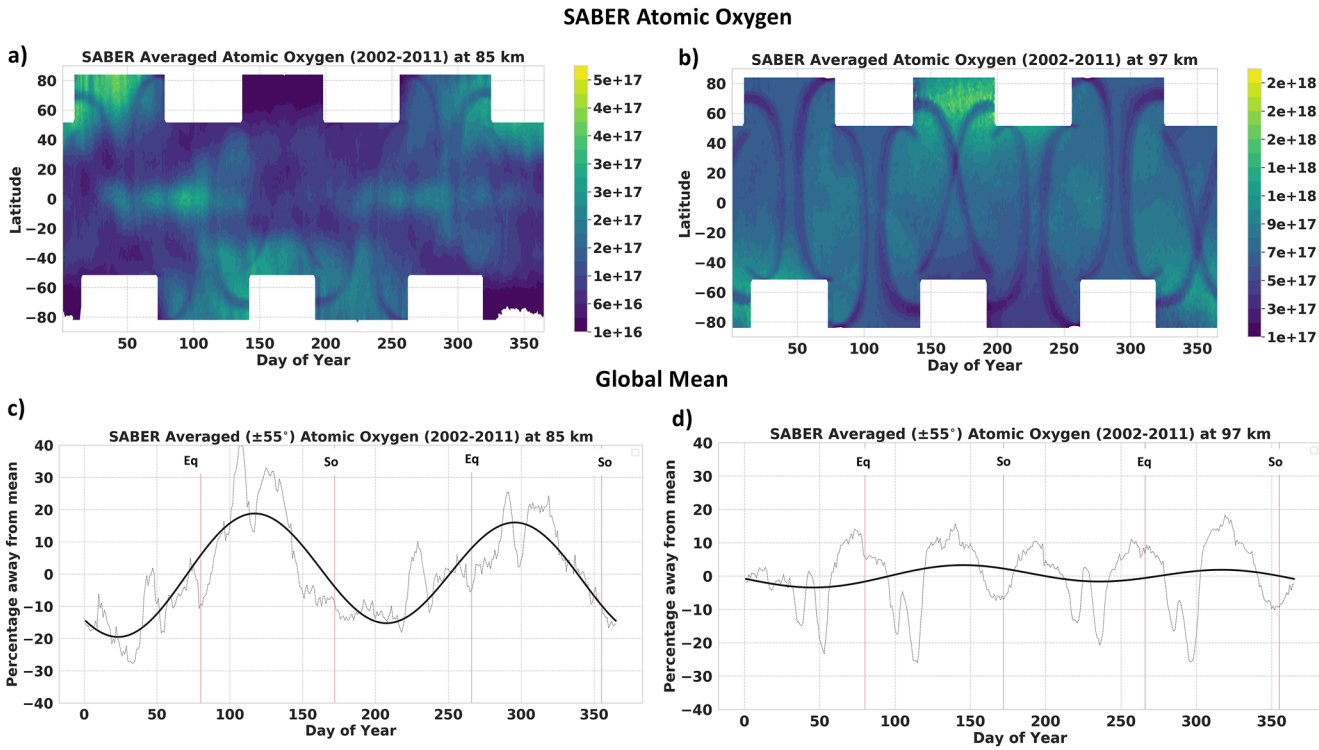

Figure 2. [O] for Sounding of the Atmosphere using Broadband Emission Radiometry in m^{-3}, averaged for 2002–2011, binned by day of the year and latitude (a) at 85 km, (b) at 97 km. Area-weighted normalized global means spanning ±55° (c) at 85 km, and (d) 97 km.

average is dominated by the SAO with maxima closer to the equinoxes. This is because the high latitude AO in both the hemispheres is out of phase and cancels out, which then reinforces the lower latitudinal SAO in the global means.

At 97 km, the AO at higher latitudes reverses with larger [O] during the summer (Malhotra et al., 2020; J. P. Russell et al., 2004; Smith et al., 2010; Sheese et al., 2011). The mechanism responsible for these summer maxima is still under investigation (Qian et al., 2017; Malhotra et al., 2020; Rezac et al., 2015; Smith et al., 2010). The effect of this reversal on the upper thermosphere was discussed by Malhotra et al. (2020). It can also be observed that the SAO at 97 km at lower latitudes is almost nonexistent and is smaller than that observed by Smith et al. (2010). This difference might arise because of different years that are included in the averages or different versions of SABER data. In Figure 2d, small intra-annual variation is observed with maxima around solstices in the global mean [O]. The high latitude AO in the two hemispheres do not completely cancel each other out, resulting in net maxima closer to the solstices. It should be noted that these plots represent averaged values over a 10 year period. The global averages for individual years can have deviations from this average. The amplitude of smoothed intra-annual variation is ∼20% at 85 km and decreases to <∼3% at 97 km. Note that if high latitude SABER data are also included in the calculation of global average [O], this amplitude increases and SAO peaks a little later in the year.

Figures 3a and 3b illustrate the latitudinal distribution of [O] at ∼97 km from MSIS and WACCM-X in 2010, respectively. WACCM-X shows more temporal and spatial variations, which is indicative of atmospheric variations including gravity waves, non-migrating tides, and planetary waves propagating up from the lower atmosphere. The latitudinal distribution of [O] in WACCM-X matches better with the SABER data at 97 km in Figure 2b. Both show annual variation at higher latitudes with maxima in summer and minima in winter. MSIS, on the other hand, has higher [O] during winter. This is because the [O] for MSIS in the MLT is extrapolated from higher altitudes assuming mixed equilibrium below the turbopause (∼105 km) with a correction factor for chemistry and dynamics. The version of MSIS used here, NRLMSISE-00 did not have [O] observations in the MLT region as SABER

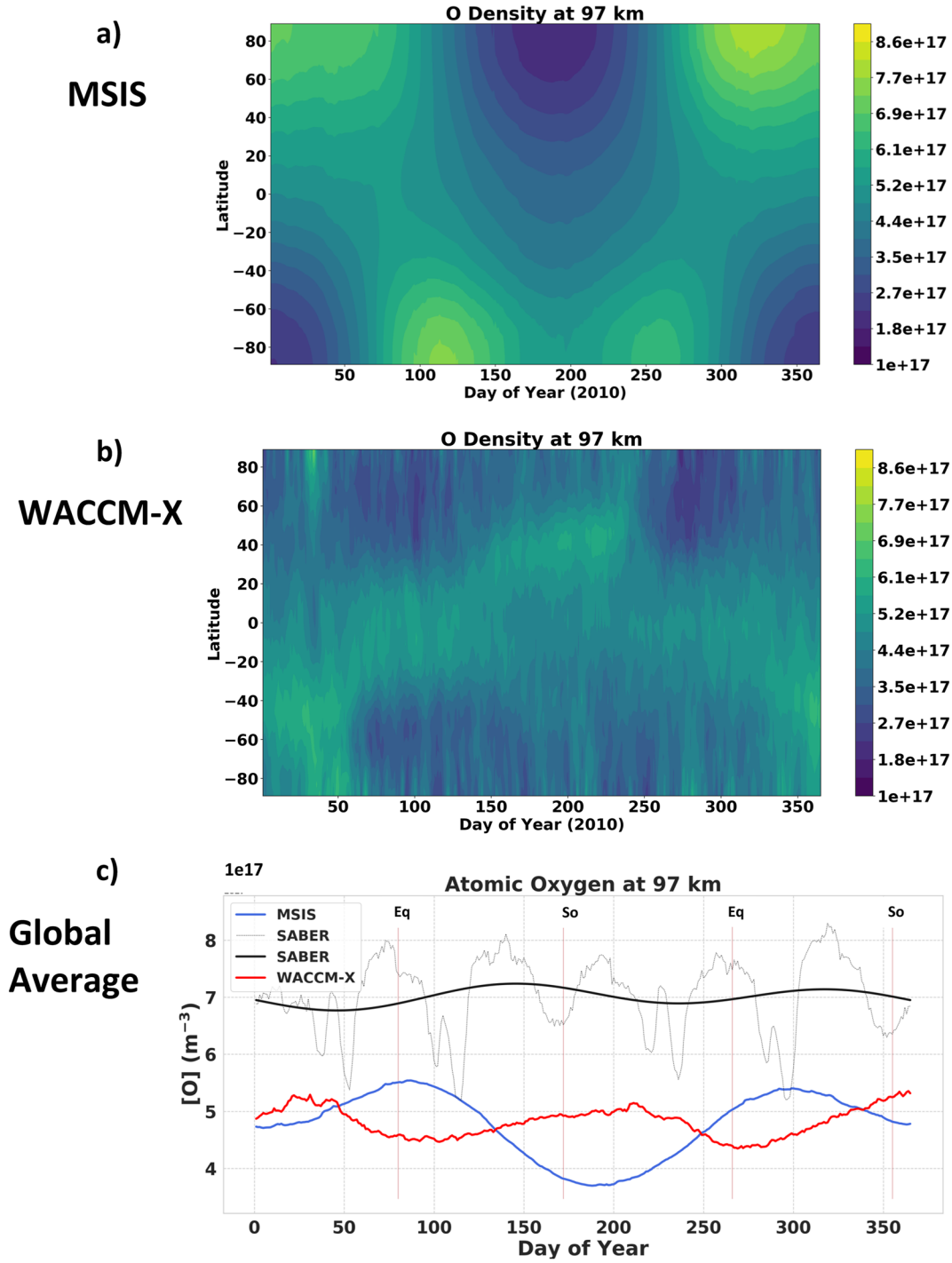

Figure 3. Diurnally averaged [O] in m^{-3} for 2010 for (a) MSIS and (b) whole atmosphere community climate model with thermosphere and ionosphere extension at 97 km. (c) Area-weighted globally and diurnally averaged [O] at 97 km. For Sounding of the Atmosphere using Broadband Emission Radiometry (SABER), the thin black line indicates the raw data and the thicker black line indicates the fitted values. SABER data are similar to that of Figure 2 and thus is the long-term average for 2002–2011.

had not been launched when it was created. Most of the observations in this region are of neutral densities and temperature from rockets and incoherent scatter radars. Therefore, the correction factors in MSIS do not account for the processes responsible for high latitude summer [O] in the MLT. The summer MLT maximum in [O] at

high latitudes is better represented in NRLMSIS 2.0 (see Figure 11 of J. T. Emmert et al., 2020). At low latitudes, WACCM-X and MSIS show a larger amplitude SAO than what SABER observed. A possible explanation for this might be the larger uncertainty in SABER [O] at these altitudes (Mlynczak et al., 2013; Smith et al., 2013).

Figure 3c compares the area-weighted global mean [O] for MSIS, WACCM-X, and SABER data at 97 km. The [O] for MSIS and WACCM-X is for 2010, whereas the SABER data are the average for 2002–2011 shown previously in Figure 2d. The global mean [O] for both SABER and WACCM-X shows an SAO with maxima closer to solstices, whereas, [O] for MSIS shows an SAO with 180° phase shift (maxima around equinoxes). In MSIS, the high latitude AO in both the hemispheres cancels out with each other resulting in minima at solstices. For WACCM-X, at equinoxes, low [O] at mid-to-high latitudes result in minima at equinoxes relative to solstices. The SAO amplitude is lower and also in agreement between WACCM-X and SABER. The overall magnitude of [O] for SABER, however, exceeds that of both MSIS and WACCM-X. Note, NRLMSIS 2.0 [O] at 97 km is roughly a factor of 2 higher than what is shown in Figure 3c (see J. T. Emmert et al., 2020, Figures 11–13).

Since, the latitudinal distribution of [O] for WACCM-X is similar to SABER, the lower boundary of GITM was changed to WACCM-X in 2010 to assess its effects on the T-I SAO. We cannot directly use SABER at the lower boundary of GITM because of the lack of measurements at high latitudes. As specified in Section 2, we also use other parameters from WACCM-X in GITM. The temporal and latitudinal variation for these parameters are not much different between MSIS and WACCM-X, and are shown in the Supporting Information S1. Therefore, our results primarily signify the implications of different [O] distribution at the lower boundary. In the next few sections, we will analyze the results of different simulations, starting with a comparison of meridional winds in the thermosphere.

3.3. Dynamics

Figure 4 shows the 16-day averaged meridional winds for HWM, WACCM-X, and different GITM simulations at June solstice (June 21 $\pm$ 8 days). We take a multiday average to eliminate short-term variations due to tides and planetary waves, such that the winds in this figure represent background meridional winds. All GITM simulations except G/NUDGE show a higher altitude summer-to-winter thermospheric circulation starting from around ~140 km which roughly agrees with HWM and WACCM-X winds, although both HWM and WACCM-X have larger wind speeds at summer high latitudes. G/NUDGE shows equatorward winds between 140 and170 km and summer-to-winter winds above 170 km. The wind patterns in the lower thermosphere are much different between the different model runs. In the lower thermosphere, between 100 and 120 km, two equatorward circulation cells are observed in G/NOSAO, G/MSIS, and G/WX simulations. These circulation cells are observed in GITM throughout the year and were shown to be driven by the centrifugal force (Malhotra et al., 2020). Comparing Figures 4d and 4e, we see that changing the lower boundary from MSIS to WACCM-X affects the magnitude of the winds in the lower thermosphere, but does not change their direction. HWM and WACCM-X winds, on the other hand, show a region with winter-to-summer circulation which has previously been observed to be caused by residual gravity waves during solstices (Qian et al., 2017). HWM primarily has Wind Imaging Interferometer (WINDII) data in this altitude regime. Being a global T-I model, GITM does not resolve gravity waves. Therefore, it does not have the requisite forcing for this opposite lower thermospheric circulation and hence, relies on realistic boundary conditions. G/NUDGE demonstrates the effect of constraining the winds in GITM with WACCM-X up to 140 km. Between 100 and 120 km, G/NUDGE shows weak winter-to-summer circulation similar to pure WACCM-X and HWM.

As an aside, during equinoxes (not shown here), GITM simulations continue to show the equatorward circulation cells below 120 km. During this time, HWM and WACCM-X also show a similar circulation pattern. This has also been previously observed in the High Resolution Doppler Imager (HRDI) and WINDII wind measurements onboard the Upper Atmosphere Research Satellite (McLandress et al., 1996; Zhang et al., 2007). It is possible that, because of absence of strong residual gravity wave forcing during equinoxes, the centrifugal force dominates the momentum budget in this region at equinoxes, resulting in net equatorward winds in the lower thermosphere.

Figure 5 shows the 60-day-averaged meridional wind for TIDI data near December and June solstices. In Figure 5a, between 90 and 100 km, northward winds indicate the mesopause summer-to-winter circulation during December solstice. The horizontal line at 97 km indicates the lower boundary of GITM. Above 100 km, southward winds depict the winter-to-summer residual circulation. Similar meridional wind patterns are also observed

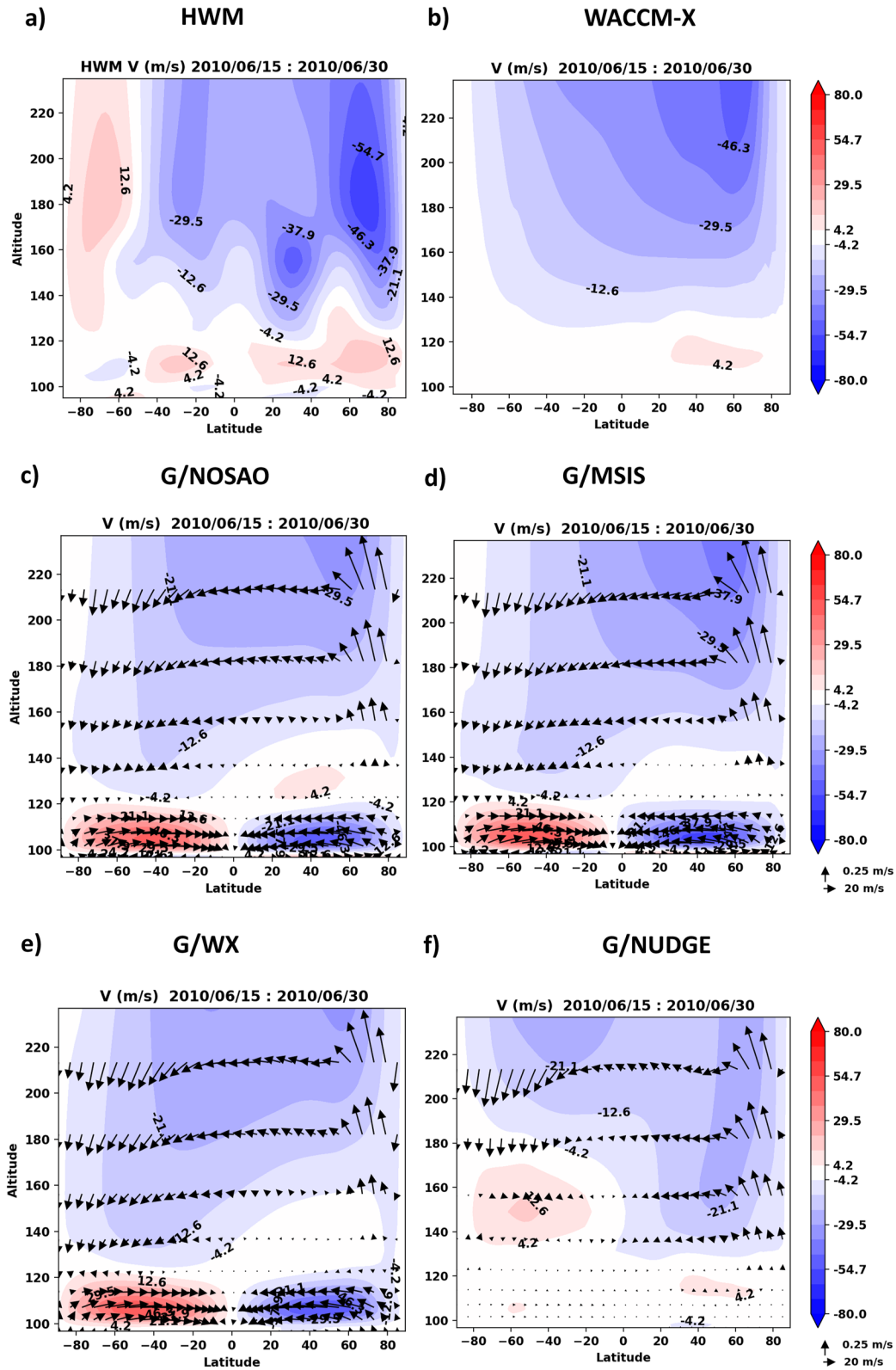

Figure 4. Latitude-Altitude cross section of zonally and diurnally averaged meridional winds in *m/s* for 2010/06/15–2010/06/30 for (a) Horizontal Wind Model, (b) whole atmosphere community climate model with thermosphere and ionosphere extension, (c) G/NOSAO, (d) G/MSIS, (e) G/WX, and (f) G/NUDGE. The negative values depict southward winds. Vectors indicate a sum of meridional and vertical winds (scaled by × 50).

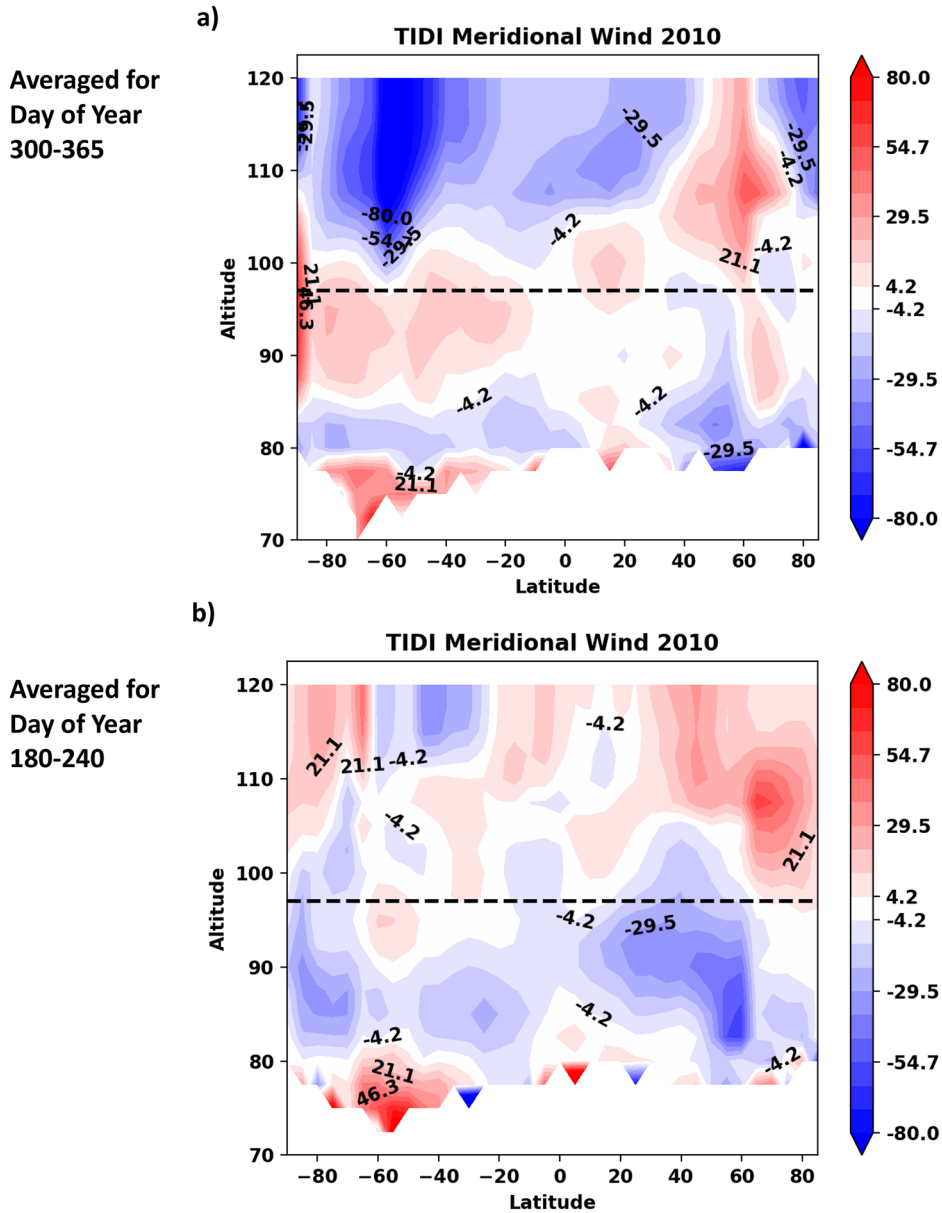

Figure 5. Averaged meridional winds in *m/s* for TIMED Doppler Interferometer binned by latitude and altitude for days of the year (a) 300–365 and (b) 180–240 in 2010. The dashed black horizontal line indicates the altitude of lower boundary of GITM, ~97 km.

during June solstice in Figure 5b in the opposite direction, potentially signifying an AO in meridional winds in the lower thermosphere. Recently, Dhadly et al. (2020) showed similar oscillations at midlatitudes, as well as an SAO, and high order intra-annual oscillations in middle thermospheric in situ measurements of the horizontal neutral winds from the Gravity Field and Steady-State Ocean Circulation Explorer (GOCE) accelerometer. HWM and WACCM-X agree with the TIDI data between 100 and 120 km, and thus nudging the GITM dynamics toward WACCM-X should improve the thermospheric modeling and SAO in GITM. However, it is worth noting that the magnitude of the winds in the winter-to-summer circulation is much larger in TIDI data during both solstices. In the next section, we will reveal the effect of different thermospheric dynamics on the amplitude and phase of T-I SAO of the simulations.

3.4. Global Mean Intra-Annual Variations

Figure 6 reveals the averaged normalized O/N_2, TEC, and [O] and ρ at ~400 km for GITM simulations compared with different data sets and models for 2010. This comparison was shown for G/NOSAO and G/MSIS previously in Figure 1. Similar to Figure 1, thin lines are the daily averages for all data and the thicker lines indicate fitted values. The parameters are normalized with respect to annual means as specified in Equation 5. The amplitudes and phases for different model runs and observations are also summarized in Table 2.

Figure 6a shows the daily averaged and fitted O/N_2. The black line represents the averaged O/N_2 measurements from GUVI data. The phase of the SAO in G/MSIS and G/NOSAO matches best with the GUVI data and the MSIS model, with equinoctial maxima. Using MSIS at the lower boundary (G/MSIS) is, however, not enough, as it produces a smaller SAO amplitude in comparison to GUVI observations. While WACCM-X [O] compares well with SABER in the MLT, using WACCM-X at the lower boundary of GITM (G/WX) leads to a T-I SAO with maxima closer to solstices and a phase difference of ~180° from GUVI SAO. Using dynamics from WACCM-X in the lower thermosphere (G/NUDGE) reduces the amplitude of this out-of-phase SAO, but does not completely correct it.

The phase shifts and amplitudes in TEC, and globally averaged [O] and ρ in Figures 6b–6d show similar model differences as the O/N_2, with maxima and minima for G/WX and G/NUDGE almost midway between solstices and equinoxes. At 400 km, the major neutral constituent is O, and thus, ρ primarily represents variations in [O]. However, for neutral density at 400 km, there are more observational data sets to validate the simulations against. The densities from Emmert data set, CHAMP, and GRACE peak around equinoxes (with an equinoctial asymmetry) similar to that of G/NOSAO and G/MSIS. The difference in phase of both G/WX and G/NUDGE simulations with respect to G/MSIS in Figures 6b–6d is lower when compared to that for O/N_2 in Figure 6a. This hints toward phase progression of SAO with altitude in G/WX and G/NUDGE simulations toward equinoctial maxima due to the effect of temperature and possibly the thermospheric spoon mechanism. This can also be noted by comparing the day of first maxima of G/WX and G/NUDGE simulations for different quantities in Table 2. The summer-to-winter meridional wind speeds increase with altitude in the lower-middle as shown in Figure 4, resulting in decrease of global mean solstitial densities relative to equinoctial densities. This will be more clear in Figure 7 where we show variations in phase of SAO with altitude.

The WACCM-X model also has an SAO that is out-of-phase in the lower thermosphere as seen in O/N_2 (Figure 6a). However, it has the correct phase in TEC, [O], and ρ at 400 km, with peaks at the equinoxes. This implies that the phase shifts toward equinoctial maxima in the lower-middle thermosphere. Nudging GITM dynamics to WACCM-X up to 140 km reduces the amplitude of oppositely phased SAO in G/NUDGE, but it is not enough to completely correct the phase and shift the phase to equinoctial maxima. This reduction in the amplitude of the opposite SAO signifies primarily the contribution of the lower thermospheric residual circulation. Qian and Yue (2017) showed that the residual circulation results in upwelling and reduction of O/N_2 in winter, and downwelling and its increase in summer. This leads to an overall reduction of the global mean O/N_2 by 18% during solstices. Comparison of G/NUDGE with G/WX shows a similar reduction in the global mean for all parameters in Figure 6 around both June and December solstices. Further explanation of these differences is beyond the scope of this manuscript.

Figure 7 compares the altitudinal progression of the [O] and ρ SAO amplitudes and phases. For [O] at 100 km, MSIS and G/MSIS have the largest amplitude of 15%, with maxima at around equinoxes (day 100). Both G/WX, G/NUDGE, and the WACCM-X model start with a much lower amplitude of around 5%, with maxima near solstices (day 10), which are in better agreement with the amplitude and phase of SABER data at 100 km. G/NOSAO starts with an amplitude of ~0. WACCM-X shows a minimum at around ~120 km, above which the amplitude increases monotonously. The amplitude of SAO in WACCM-X remains lower than other simulations also causing much lower amplitude in G/NUDGE, at ~10%–15%. WACCM-X transitions from solstitial maxima to equinoctial maxima in the 100–200 km altitude region. In the upper thermosphere, G/MSIS, G/NOSAO, and G/WX have the largest amplitudes of ~25%, which is greater than that of MSIS. Since, there are limited observations of [O] in the thermosphere, there is an uncertainty regarding which simulation represents the correct SAO amplitude. A similar amplification of the SAO with altitude for different neutral species was depicted by Picone et al. (2013) because of the variation in temperature. Thus, it is possible that different temperature structure between the simulations leads to different amplification factors of the SAO. When considering the importance of SAO at the lower

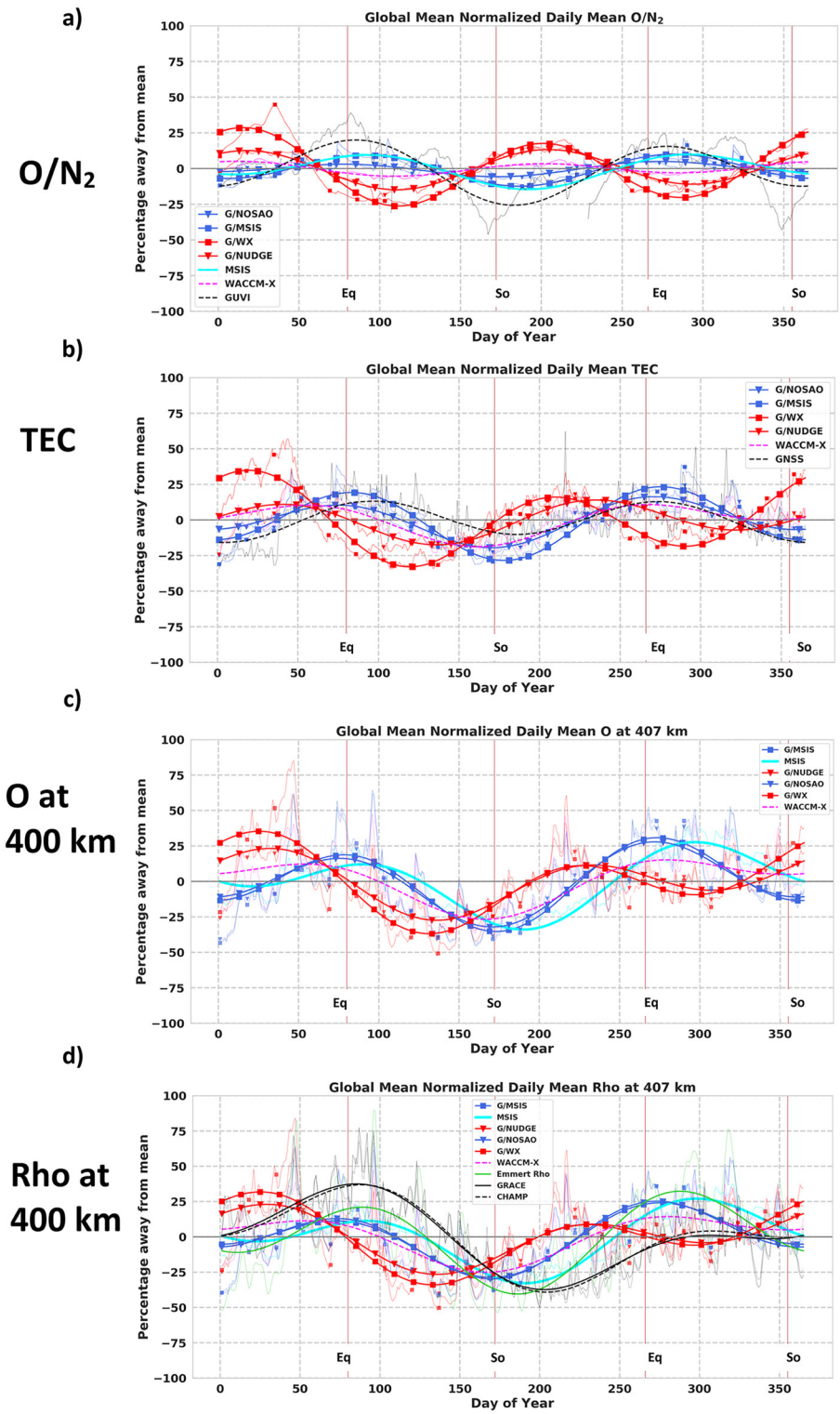

Figure 6. Diurnally averaged, normalized (area-weighted) global means (a) O/N_2, (b) Total Electron Content, (c) [O] at 407 km, and (d) ρ at 407 km, for different Global Ionosphere Thermosphere Model simulations, whole atmosphere community climate model with thermosphere and ionosphere extension model, MSIS, and observational data sets. The thin lines indicate the raw data and the thicker lines indicate the fitted values. Similar to Figure 1, Challenging Minisatellite Payload (CHAMP) and Gravity Recovery and Climate Experiment data sets are normalized to 400 km and averaged for 2007–2010. The red vertical lines indicate the days of equinoxes and solstices. The gray horizontal lines at 0 indicate the zero change lines.

Table 2
Semiannual Oscillation (SAO) Amplitude and Phase for Different Model Runs and Observations

	ρ at 400 km		O/N_2		TEC	
Model run	SAO amplitude (%)	SAO phase	SAO amplitude (%)	SAO phase	SAO amplitude (%)	SAO phase
G/NOSAO	18.2	82	3.9	84	12.9	81
G/MSIS	16.6	83	9.6	95	21.0	87
G/WX	18.9	34	23.1	16	25.2	22
G/NUDGE	14.9	38	12.9	19	12.2	46
WACCM-X	10.0	76	4.2	14	9.4	70
MSIS	17.5	104	9.3	100		
GRACE	16.2	97				
CHAMP	17.3	101				
Emmert Data set	25.6	97				
GUVI			18.2	89		
GNSS					12.9	95
TIE-GCM, w/Q09	16.2	122			26.5	129
TIME-GCM Standard	12.8	114			19.7	106

Note. The amplitude is determined by fitting a least squares semiannual variation to the data. Phase is the day of first maxima. Thermosphere Ionosphere Electrodynamics General Circulation Model (TIE-GCM) and TIME-GCM values are from Jones et al. (2017).

boundary, G/NOSAO catches up with other simulations above 300 km. However, the absence of lower boundary SAO results in much smaller amplitude below 300 km. Hence, our results indicate that it is necessary to have an SAO in composition and winds at the lower boundary of T-I models for better agreement with the observations in the lower-middle thermosphere, otherwise it can lead to underestimation of the SAO in this region. Recent work by Jones et al. (2021) using the TIE-GCM showed that including NRLMSIS 2.0 composition improved the globally averaged mass density SAO at 400 km in the TIE-GCM (although the TIE-GCM amplitude was notably smaller than observed).

The phase for [O] largely remains constant with altitude for all GITM simulations. G/MSIS and G/NOSAO continue to have maxima at equinox in the upper thermosphere, which leads the MSIS SAO, as observed previously in Figure 1c. G/WX and G/NUDGE have maxima near the solstices progressing toward equinoxes with altitude. As stated before, we believe that this is due to the effect of temperature and the summer-to-winter thermospheric circulation that pushes the thermosphere toward a more mixed state at solstices. This phase progression is most apparent between 100 and 300 km, above which it does not change much. This is because the thermospheric spoon mechanism is more dominant in this altitude region. Above ~300 km, O is in diffusive equilibrium and thus the SAO phase is constant at higher altitudes.

Figure 7b shows the variation of SAO phase and amplitude for ρ. Above 200 km, O is the major species and hence the SAO in ρ primarily reflects the variations in [O]. At 100 km, all the simulations start with a maxima at ~day 90 (equinox) because of the dominance of the N_2 density. The SAO in ρ for G/MSIS and G/NOSAO has almost a constant phase with altitude displaying an equinoctial maxima, fairly consistent with MSIS and TIME-GCM simulations by Jones et al. (2017). Pure WACCM-X also exhibits a constant SAO phase above 100 km, peaking at equinox. This is because of the dominant equinoctial maxima in N_2 in the lower-middle thermosphere and equinoctial maxima in [O] above 200 km. In G/WX and G/NUDGE, the phase shifts from equinoctial (due to N_2) toward solstitial maxima at ~200–250 km (because of O). The model runs that show the correct phase, that is, the equinoctial peaks (WACCM-X, G/MSIS, and G/NOSAO), lead all observational data sets (MSIS, CHAMP, GRACE, Emmert data, and GOCE). These observational data sets peak at a similar time around ~day 100, while model simulations peak at ~day 80 (also in Table 2). The SAO amplitude for ρ increases with altitude similar to that of [O]. The SAO amplitude for the GITM simulations reaches a maximum of ~20% and is in better agreement with CHAMP and GRACE, whereas the amplitude is much larger in the Emmert and GOCE data. The SAO

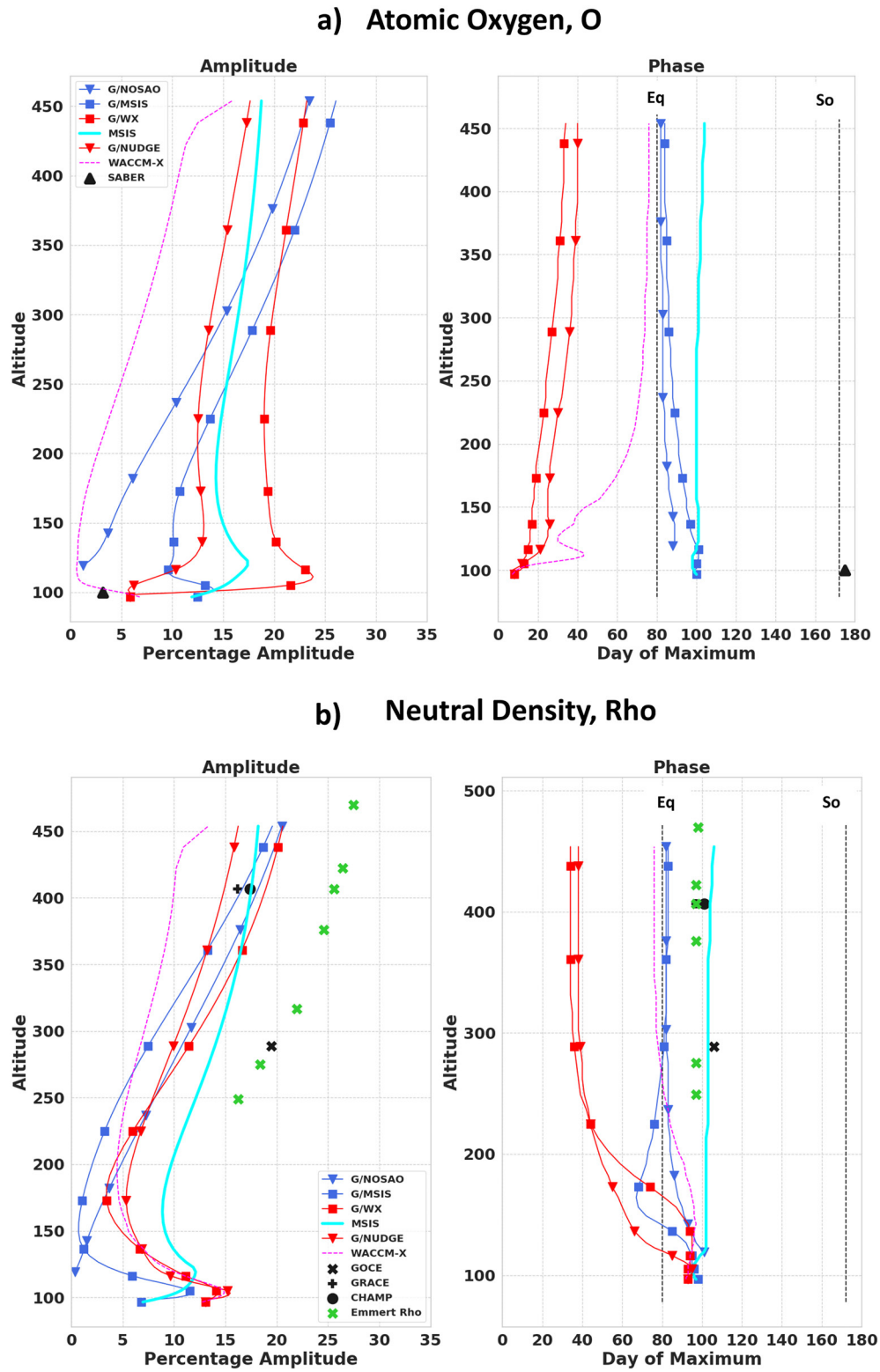

Figure 7. Semiannual oscillation (SAO) Amplitudes and phases with altitude for (a) [O] (b) ρ, for different Global Ionosphere Thermosphere Model simulations, whole atmosphere community climate model with thermosphere and ionosphere extension model, MSIS, and observational data sets. SAO Amplitudes and phases are calculated from least squares fits to normalized daily averages of Figure 6. The phase signifies the day of first maximum. The vertical dashed black lines indicate the day of equinox (March 21) and solstice (June 21).

in temperature at 400 km (not shown here) has an amplitude of ∼<3%, maximizing around ∼day 70–80 for G/NOSAO and G/MSIS and ∼day 50–60 for G/WX and G/NUDGE.

In summary, using WACCM-X [O] instead of MSIS at the lower boundary in GITM, leads to the phase of T-I SAO that does not agree with the observations, despite the SABER-like [O] distribution at the lower boundary. This can be linked with the solstitial peaks in the global mean of [O] at 97 km in WACCM-X. Even though, O is not in diffusive equilibrium above 97 km, but in fact is driven by the dynamics and chemistry in the lower thermosphere, the phase shift in SAO between the MLT and upper thermosphere is marginal. The maximum change in the phase of SAO in global mean [O] in GITM between the lower boundary and upper thermosphere is ∼30 days, and thus is not enough to drive a seasonal change in the phase of SAO, that is, from solstices to equinoxes.

A similar analysis was done by Jones et al. (2017); see Figure 2 for different TIME-GCM simulations. Table 2 shows the SAO amplitudes and phases for standard TIME-GCM and TIE-GCM with Qian et al. (2009) eddy diffusion variation (TIE-GCM w/Q09). Comparing with our G/MSIS simulation, for both TEC and ρ at 400 km, G/MSIS peaks earlier in the year (day 83) as compared to these two simulations from Jones et al. (2017); day 106 and 122. The phase of the observations (GPS, CHAMP, GRACE, and Emmert data set) lies between these different models. For the SAO amplitudes, these three model runs have larger amplitudes than the GNSS TEC (∼13%). Comparing the ρ at 400 km, both TIE-GCM w/Q09 and G/MSIS agree with the SAO amplitude of CHAMP and GRACE (∼16%–17%). To further understand the differences between our simulations, we will analyze the latitudinal distribution of thermospheric densities in the next section.

3.5. Global Distribution

Figure 8 illustrates the latitudinal distribution of [O] at ∼150 km. G/NOSAO and G/MSIS show a similar variation, with equinoctial maxima at lower latitudes. At solstices, larger [O] is observed in the winter hemisphere because of the interhemispheric summer-to-winter circulation. At ∼day 180, by comparing the summer minima in the northern hemisphere between these two simulations, we see that G/MSIS has a minima spanning a larger latitudinal region. Similar behavior is observed starting from ∼day 350 in the southern hemisphere. This is because G/MSIS starts with the summer minima and winter maxima at the GITM lower boundary (see Figure 3). The interhemispheric circulation adds to this depletion in summer and accumulation in winter. This can result in an underestimation and overestimation of [O] in summer and winter, respectively (Malhotra et al., 2020).

G/WX and G/NUDGE also show winter [O] accumulation. Thus, GITM is able to reverse the opposite latitudinal variation of [O], from larger values in the summer at ∼97 km to relatively larger values in winter at ∼150 km. There is also an increase in summertime [O], and thus decrease in the summer-to-winter gradient at solstices similar to G/NOSAO. The features of primary importance in these Figures 8c and 8d are the low latitude maxima at solstices that contribute to the global mean T-I SAO that is almost oppositely phased with respect to the observations and G/MSIS (shown in Figure 6). G/NUDGE has a similar latitudinal distribution as G/WX, but the absolute [O] densities are much larger for both equinoxes and solstices. This is primarily because of the weakening of equatorward circulation cells below 120 km, during both solstices and equinoxes. To zeroth order, these circulation cells can be viewed as a "large-scale eddy" mixing the thermosphere, thereby decreasing light species concentration (i.e., O) and increasing heavy species concentration (i.e., N_2), almost equally throughout the year, resulting in minimal effect on the SAO amplitude and phase. In Figure 6, the parameters were normalized, leading to an overall decrease of the SAO amplitude in G/NUDGE due to the contribution of the residual circulation as discussed previously. In contrast with Figures 8c and 8d, the WACCM-X model in Figure 8e exhibits stronger winter maxima. However, similar to both G/WX and G/NUDGE simulations, the summer-winter gradient is low. [O] from MSIS is shown here for consistency. We do not expect MSIS to have the correct distribution at these altitudes because of the lack of [O] observations. It shows deep summer minima at mid-high latitudes that cancels out the winter maxima of the opposite hemisphere, resulting in equinoctial peaks in the global means.

Figure 9 shows neutral density at ∼400 km (resembles major species, [O] at 400 km) from all our model simulations, as well as CHAMP and GRACE observations. The high latitude winter maxima observed for [O] at ∼150 km has transitioned to high latitude summer maxima at ∼400 km in this figure. This is because above ∼300–400 km, the effect of larger summer temperatures dominates over that of compositional changes (due to thermospheric spoon mechanism) at a constant altitude (J. Emmert, 2015). The ρ for G/WX and G/NUDGE have the correct annual oscillation at high latitudes, however, the maxima at lower latitudes are at solstices, similar to

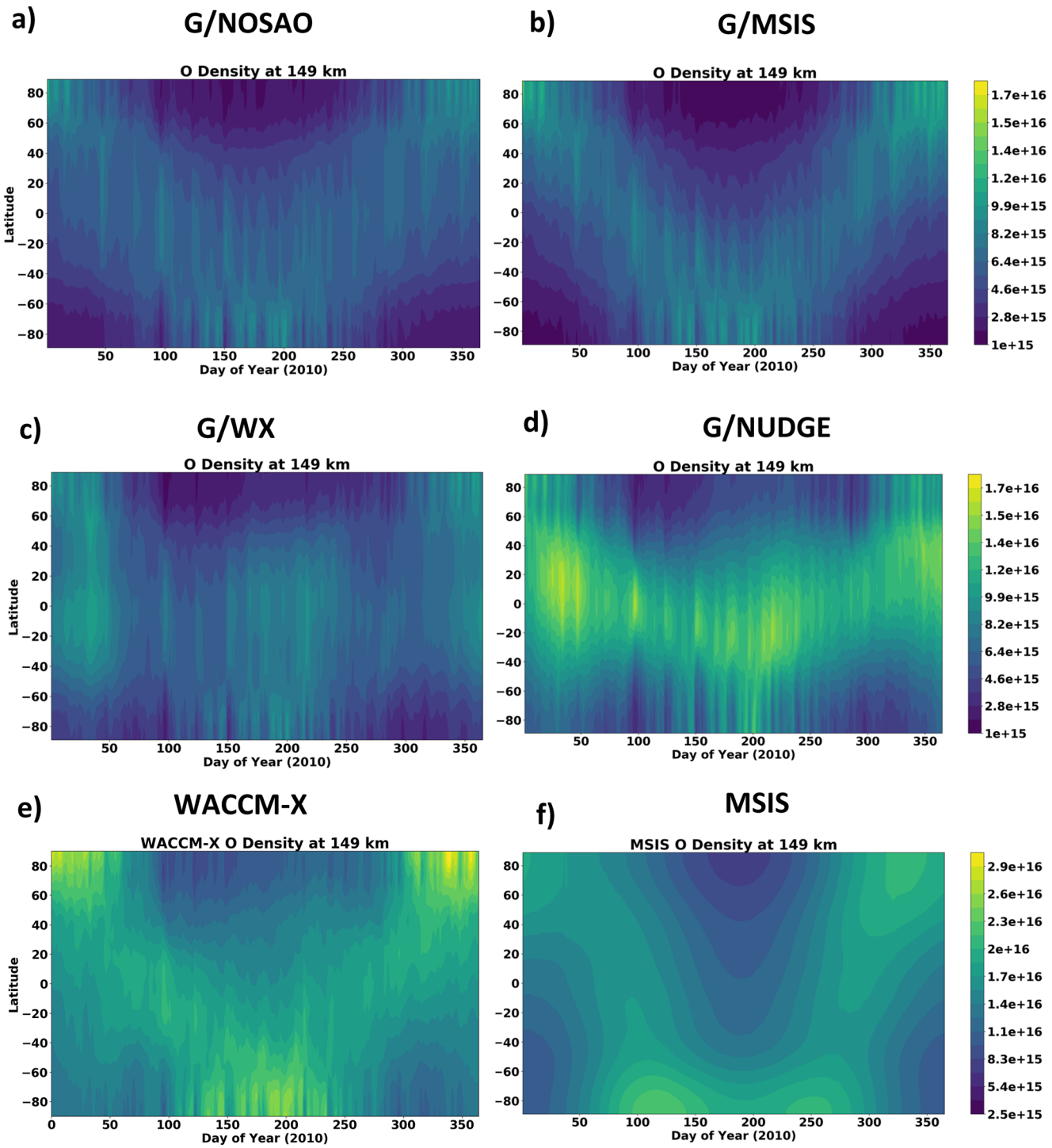

Figure 8. Diurnally averaged distribution of [O] with latitude in m^{-3} at 149 km for 2010 for (a) G/NOSAO, (b) G/MSIS, (c) G/WX, (d) G/NUDGE, (e) whole atmosphere community climate model with thermosphere and ionosphere extension, and (f) MSIS empirical model.

[O] at ~150 km. Thus, the intra-annual variation in [O] stays the same at lower latitudes above ~150 km. The latitudinal distribution of G/NOSAO and G/MSIS agrees with MSIS, CHAMP, and GRACE data, with slight phase differences. Comparing the absolute values of [O] and ρ in Figures 8 and 9, it should be noted that the difference among the various GITM simulations is largest during solstices. Thus, major phase differences between

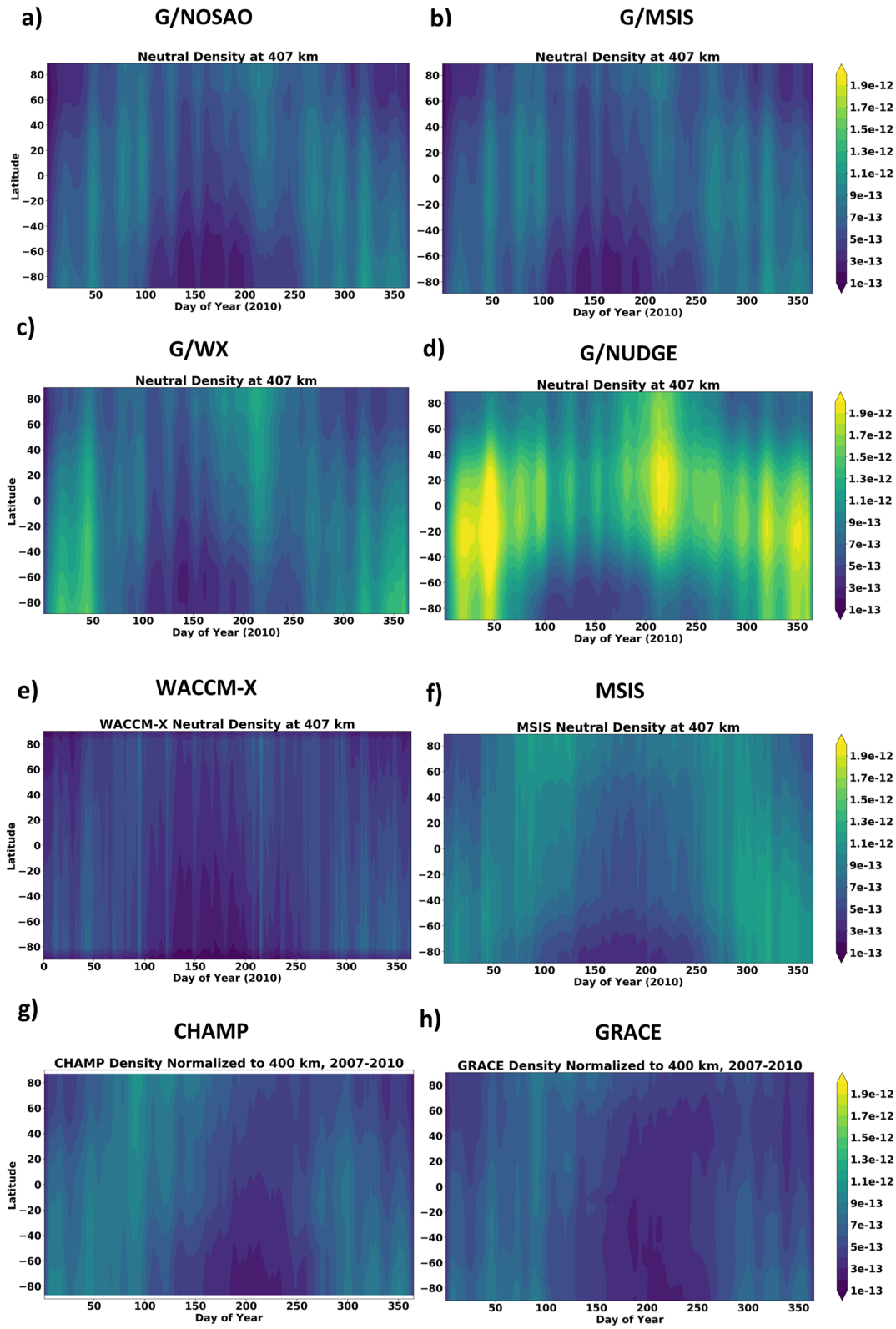

Figure 9. Diurnally averaged distribution of ρ with latitude in m^{-3} at 400 km for (a) G/NOSAO, (b) G/MSIS, (c) G/WX, (d) G/NUDGE, (e) whole atmosphere community climate model with thermosphere and ionosphere extension, and (f) MSIS empirical model. (g) Challenging Minisatellite Payload (CHAMP), (h) Gravity Recovery and Climate Experiment (GRACE). CHAMP and GRACE data sets are normalized to 400 km and averaged for 2007–2010.

the global means of the simulations in Figure 6, arise because of a relative increase in low latitude [O] during solstices in the lower thermospheric altitude region in G/WX and G/NUDGE.

Note that the results in a previous study by Malhotra et al. (2020) showed that using high summer [O] from WACCM-X at the lower boundary improves the O/N_2 agreement of GITM with the GUVI data during January and June. The WACCM-X driven GITM simulation showed a decreased O/N_2 gradient between the two hemispheres. We observe similar results in this study in Figure 8. However, since that study covered only a small number of days around the solstices, the wrong phase of global mean T-I SAO was not inferred. This raises the question, if WACCM-X represents the MLT state more accurately, how and why does the phase of T-I SAO in G/WX and G/NUDGE not agree with observations? What are the additional processes in the lower thermosphere that are required to correct this discrepancy? We will henceforth look at the differences between the simulations during June solstice, when they are the largest.

3.6. June Solstice

The panels on the left in Figure 10 show the averaged latitude-height distribution for temperature, whereas the panels on the right show the latitudinal gradient in temperature, for GITM simulations and WACCM-X around June solstice. Positive temperature gradient signifies larger temperature toward north (summer) and vice-versa. We show only G/MSIS and G/WX simulations here because G/MSIS shows a similar distribution as the G/NOSAO, and G/NUDGE is similar to WACCM-X. Overall, thermospheric temperature is larger in GITM than in WACCM-X. In the lower thermosphere, between 100 and 120 km, GITM shows low temperatures at high latitudes. This is because of the divergence and adiabatic cooling due to equatorward circulation cells shown in Figure 4.

Above 140 km, WACCM-X has the weakest temperature gradient between the two hemispheres. It shows positive temperature gradient at all heights. GITM on the other hand shows a large positive gradient in both the hemispheres. As compared to G/MSIS, the gradient is slightly lower at equatorial latitudes in G/WX. A possible explanation for this difference was discussed by Malhotra et al. (2020). As discussed in that study, high summer [O] from WACCM-X at the lower boundary of GITM changes the wind magnitudes between 100 and 120 km. This high summer [O] leads to larger equatorward winds because of relatively larger equatorward-directed force, resulting in more adiabatic cooling. Similarly, lower winter [O] produces relatively slower equatorward winds resulting in less adiabatic cooling. This effect introduced near the lower boundary of the model has implications on the temperature structure of the whole thermosphere, resulting in the lowering of the summer temperature and relative increase in the winter temperature, thereby reducing the summer-to-winter gradient. These differences in gradients have a direct implication on the meridional and vertical winds, as the effectiveness of the thermospheric spoon mechanism depends on the temperature gradient between the two hemispheres (Jones, Emmert, et al., 2018).

Figure 11 and Figure 4 demonstrate the variation in global meridional winds with altitude for different GITM simulations, HWM, and WACCM-X. Negative (positive) values imply southward (northward) winds. Depending on the altitude, the difference in wind profiles in this figure arises because of the differences in wind patterns and the global mean magnitudes. At ∼160 km, when all the model runs have summer-to-winter directed winds, the GITM simulations have weaker wind magnitudes as compared to HWM and WACCM-X. G/MSIS has stronger meridional winds than G/WX because of a larger temperature gradient at equatorial latitudes. For G/NUDGE (Figure 4), at this altitude, equatorward winds are observed, with stronger winds from summer high latitudes toward equator. These winds change to summer-to-winter interhemispheric winds at about 170 km and maintain their lower amplitude relative to other simulations. WACCM-X shows larger summer-to-winter winds compared to all model runs despite the smaller temperature gradient. It is possible that the momentum sources from sub-grid processes, for example, breaking gravity waves at ∼140 km increase the magnitude of interhemispheric winds in WACCM-X. Another possible reason for weaker GITM winds might be stronger ion drag and viscosity. Note the momentum terms that contribute to GITM meridional winds were shown in Figure 4 of Malhotra et al. (2020). They showed that WACCM-X driven GITM had smaller winter-directed pressure gradient force at low latitudes, similar to the results shown in Figure 10. In the next section, we analyze the transport terms that contribute to the distribution of [O] in the lower thermosphere and provide evidence that low latitude accumulation in G/WX

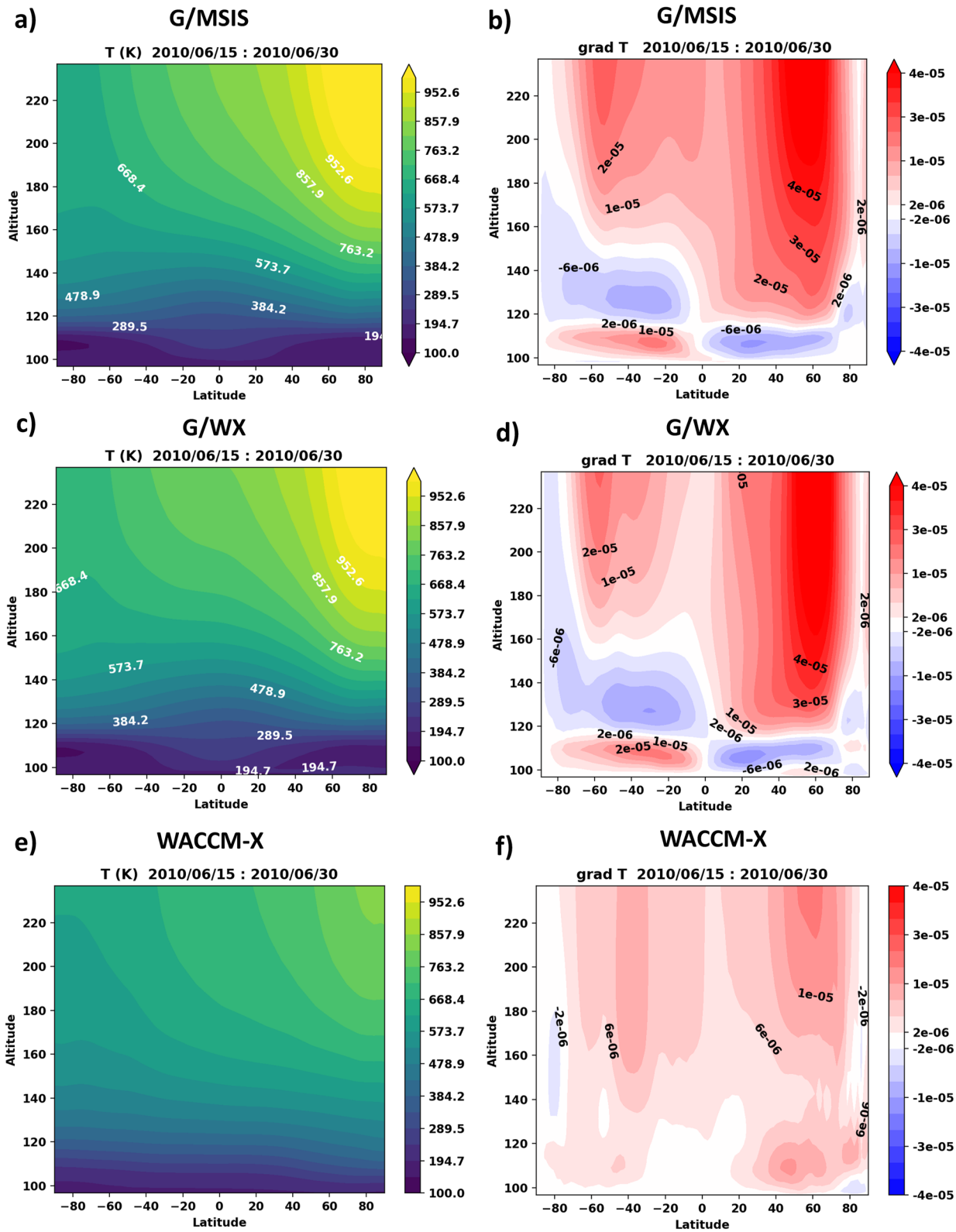

Figure 10. Latitude-Altitude cross section of zonally and diurnally averaged Temperature in *K* for 2010/06/15–2010/06/30 for (a) G/MSIS, (c) G/WX, and (e) whole atmosphere community climate model with thermosphere and ionosphere extension. Gradient in Temperature for each corresponding simulation is shown in the panel on the right. A positive gradient indicates that the temperature is larger toward the north.

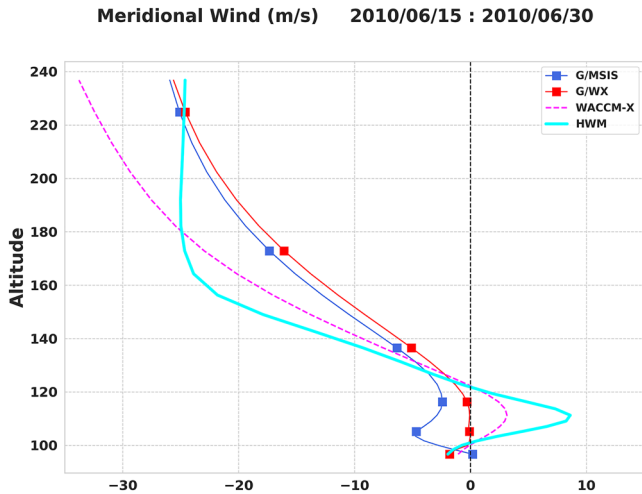

Figure 11. Globally averaged meridional winds in *m/s* for different Global Ionosphere Thermosphere Model simulations, whole atmosphere community climate model with thermosphere and ionosphere extension, and Horizontal Wind Model.

and G/NUDGE simulations are linked to weaker interhemispheric winds and mixing via the thermospheric spoon mechanism in GITM.

4. Discussion

The continuity equation in the vertical direction in GITM can be written as,

$$\frac{\partial \mathcal{N}_s}{\partial t} = -\frac{\partial u_{r,s}}{\partial r}^{*(a)} - \frac{2u_r}{r}^{*(b)} - u_{r,s}\frac{\partial \mathcal{N}_s}{\partial r}^{*(c)} + \frac{1}{N_s}S_s^{*(d)} \tag{6}$$

where,

$$\mathcal{N}_s = \ln(N_s) \tag{7}$$

following the notation from Ridley et al. (2006), r is the radial distance measured from the center of the Earth. The subscript r denotes the component in the radial direction. $u_{r,s}$ is the vertical velocity of species s. N_s is the number density of species s. The source term S_s for the species s includes the eddy diffusion and chemical sources and losses. Terms *(a) and *(b) signify the divergence of the vertical velocity and term *(c) represents the vertical advection. Here, we demonstrate these terms only for [O]. For the vertical continuity equation, we show the sum of terms *(a), *(b), and *(c). These terms collectively are referred to as the transport terms. Among the source terms, the eddy diffusion terms have a negligible effect above 120 km. Eddy diffusion acts on the thermospheric densities primarily at ∼100 km, but the effect is much smaller than the transport terms. The chemical source term for [O] shows equinoctial peaks and thus does not provide an explanation for the opposite SAO in G/WX and G/NUDGE. This is because of larger chemical loss of [O] during solstices in G/WX and G/NUDGE simulations relative to other simulations and is shown in the Supporting Information S1.

The continuity equation in the horizontal direction is:

$$\frac{\partial N_s}{\partial t} = -N_s\left(\frac{1}{r}\frac{\partial u_\theta}{\partial \theta} + \frac{1}{r\cos\theta}\frac{\partial u_\phi}{\partial \phi} - \frac{u_\theta \tan\theta}{r}\right)^{*(e)} - \left(\frac{u_\theta}{r}\frac{\partial N_s}{\partial \theta} + \frac{u_\phi}{r\cos\theta}\frac{\partial N_s}{\partial \phi}\right)^{*(f)}, \tag{8}$$

where, θ is latitude, ϕ is longitude, and the subscripts θ and ϕ denote the components in the respective directions. The first grouping on the right, labeled *(e), is the divergence term, while the second, labeled *(f), is the horizontal advection term. These are added together and considered as the horizontal transport terms below.

Figure 12 shows the latitudinal distribution of the horizontal (top panels) and vertical transport (bottom panels) terms that contribute to the global distribution of [O] at ∼150 km shown in Figure 8. The panels on the left show the terms for G/MSIS while panels on the right are for the G/NUDGE. We only show G/MSIS and G/NUDGE, as we expect similar inference for G/NOSAO and G/WX, respectively. The magnitudes are different for the vertical and horizontal terms because the vertical continuity equation uses $\mathcal{N}_s$ as shown in Equation 7. G/MSIS shows high [O] accumulation in the winter high latitudes via both horizontal and vertical transport. G/NUDGE shows weaker winter accumulation driven exclusively by vertical transport, that is, upwelling in summer and downwelling in winter. Alternatively, the horizontal transport term shows an accumulation at lower latitudes during solstices. The equatorward winds and the resulting convergence in the altitude region of 140–170 km, in addition to the weaker interhemispheric meridional winds above 170 km play an important role in the accumulation of [O] at low latitudes. The meridional wind difference between G/WX and G/MSIS shown in Figure 11 is not large enough to be solely responsible for the difference in horizontal transport shown here. Transport of [O] to low latitudes in G/WX and G/NUDGE is a consequence of a larger summer high-latitude [O] in WACCM-X accompanied by overall weaker meridional winds in GITM. G/MSIS does not have this accumulation because it already has larger winter high-latitude [O] in the MLT. It is likely that since, pure WACCM-X has larger meridional winds, it does not show equatorial accumulation of [O]. It was demonstrated by X. Liu et al. (2014) that horizontal transport similarly also affects the peak location of the winter Helium bulge.

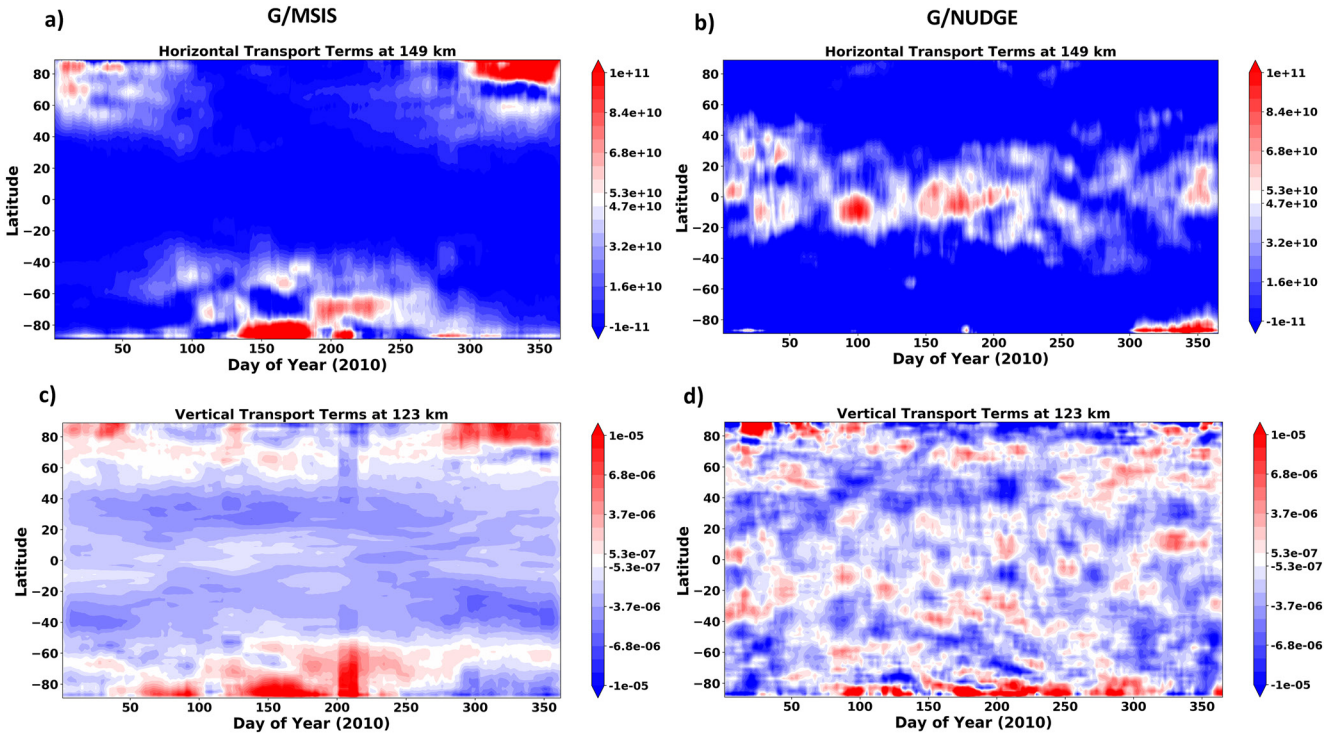

Figure 12. Diurnally averaged (15 day rolling mean) zonal means of transport terms. The panels on the left (right) are for G/MSIS (G/NUDGE). The top (bottom) panels are the horizontal (vertical) transport terms at 149 (123) km. Vertical transport terms have the units of s^{-1} and the horizontal transport terms have the units of $m^{-3}s^{-1}$.

Our results show that in GITM, when the SAO in global mean [O] in the MLT has solstitial maxima, the T-I SAO also has solstitial maxima. The low-latitude accumulation of [O] during solstices in G/WX further contributes to the increase in the SAO amplitude with altitude. From Figure 7, it is clear that the maximum change in the SAO phase for GITM runs is ∼30 days, which is not enough to bring a seasonal change in the global mean SAO of G/WX and G/NUDGE. For achieving the equinoctial maxima in the thermosphere (to match observations), either the MLT SAO should have equinoctial maxima (G/MSIS) or the global mixing in the lower thermosphere during solstices should be strong enough to decrease the [O] below its equinoctial values. G/MSIS has the right phase of the T-I SAO in the lower thermosphere because it already has larger global mean [O] at equinoxes at the lower boundary. The thermospheric spoon mechanism is enough to lead to the correct phase in G/NOSAO, but of lower amplitude in O/N_2. Since, we assume that G/WX and G/NUDGE better represent the MLT dynamics (match with SABER observations), there should be additional mechanisms acting in the lower thermosphere (not included in GITM) that decrease the solstitial [O]. Note, we also interpret similar results for January solstice (not shown here). The major difference between January and June is that the meridional wind magnitudes are much weaker for January relative to June.

It can be suggested that since WACCM-X has the right SAO phase and latitudinal distribution of [O] and ρ in the upper thermosphere, the nudging altitude in GITM should be increased to above 140 km where WACCM-X wind speeds increase to achieve the right phase of SAO. However, when compared with integrated O/N_2 from GUVI (which reflects the lower T-I state at ∼140 km), WACCM-X has the wrong SAO phase (Figure 6a). Yue et al. (2019) showed that GUVI data has an SAO in both [O] and O/N_2 with equinoctial peaks, which are in phase between the lower (8.4×10^{-4} Pa) and upper thermosphere (6.35×10^{-6} Pa). Similar results were also obtained by Yu et al. (2020). We estimate 8.4×10^{-4} Pa to be ∼140–160 km. Even though the phase of the SAO is correct in WACCM-X at 400 km, it is not until 200 km that the SAO completely transitions from solstitial maxima to equinoctial maxima. GITM on the other hand is unable to correct this as it has lower meridional wind speeds. This suggests that there are mechanisms missing in both models that could be responsible for this phase transition of the SAO in [O]. Jones et al. (2017) noted that this phase transition in the global mean SAO in TIME-GCM occurs between ∼90 and100 km. The amplitude of the SAO decreases to a minimum at 90 km, which is similar to the

low amplitude observed by SABER in Figure 2d. However, the transition altitude in TIME-GCM is much lower, as we still observe solstitial maxima in SABER [O] at 97 km. Considering the results by Yue et al. (2019) and Jones et al. (2017), in order to have the right phase of the SAO in integrated O/N_2 (and match with the GUVI observations), the global SAO should transition to equinoctial maxima in the lower thermosphere below ∼140 km. However, mechanisms driving this transition are not well understood. Jones et al. (2017) also observed a similar phase reversal between 90 and 100 km in the advective flux divergence, which was represented by a combination of meridional and vertical mean transport. This provides a hint that dynamics in the lower thermosphere might be driving this transition.

Given the results shown herein, we offer the following thoughts about certain processes that can improve the amplitude and phase of the SAO in T-I models such as GITM:

1. We introduce a seasonal variation in K_{zz} at the GITM lower boundary as a possible solution, that is, similar to that used by Qian et al. (2009) in TIE-GCM. Even though seasonally varying K_{zz} decreases the O/N_2 at solstices and increases it during equinoxes, it is not enough to completely reverse the phase of the oppositely phased SAO. We also ran a simulation using WACCM-X version 2.1 at the lower boundary of GITM and got similar results as G/WX shown in this study. The temporal variation of global mean O/N_2 and ρ at 400 km for both of these simulations are provided in the Supporting Information S1
2. HWM winds have relatively larger summer-to-winter interhemispheric winds in the lower thermosphere. Thus, the lower thermospheric meridional wind magnitudes can be increased in GITM to be in better agreement with HWM. Additionally, Jones, Emmert, et al. (2018) demonstrated that the thermospheric spoon mechanism is most effective in the altitude regime where the thermosphere is transitioning from a fully mixed state to that of diffusively separated state. This can be achieved by reducing ion drag and/or viscosity in GITM, or nudging the meridional winds to HWM. The exact magnitude of winds in this region remains to be studied as more thermospheric wind observations are made over the next few decades. Larger meridional transport during solstices can potentially improve the global SAO phase and reduce the equatorial accumulation of [O] in G/WX and G/NUDGE
3. We also observe that winter-to-summer winds between ∼100 and 120 km are much larger in TIDI data than in HWM and WACCM-X. In our G/NUDGE simulation, we found that this circulation results in the lowering of global mean (normalized) O/N_2, [O], and ρ during solstices. If this residual circulation in WACCM-X and GITM is more accurately represented such that the magnitude of the winds is in agreement with TIDI data, the solstitial maxima seen in the G/WX and G/NUDGE simulations could decrease significantly

Thus, the correct lower boundary conditions for GITM should be SABER/WACCM-X-like [O], with additional mechanisms that represent the state of lower thermospheric dynamics more accurately.

5. Summary and Conclusions

The T-I SAO is a large intra-annual density (mass and plasma) variation with maxima during equinoxes and minima during solstices. It is successfully reproduced in most global whole atmosphere models. However, T-I models need estimates of the MLT state via accurate specification of lower boundary conditions for producing the right amplitude and phase of T-I SAO. This is especially difficult as there are limited global sources to validate the winds, composition, and temperature in the MLT. It has recently been shown that lower atmospheric perturbations from gravity waves and tides can affect and improve (in some studies) the modeling of T-I SAO in the global T-I models. This study explores a possible approach to improving the amplitude and phase of T-I SAO in GITM.

Our results show that GITM successfully reproduces the T-I SAO from first principles when no SAO is present at the lower boundary, however, with lower amplitude. This demonstrates that the SAO is primarily driven by the internal thermospheric horizontal and vertical transport. Using the densities and temperature from MSIS (NRLMSISE-00) and winds from HWM (HWM14) at the lower boundary improves the amplitude and phase of SAO, especially in the lower thermosphere. However, there are still some disagreements between models and data regarding its phase and amplitude. For example, summer densities are underestimated and winter densities are overestimated during solstices, and the phase of SAO in ρ at 400 km leads the observations, especially during June and September.

Another problem is that the lower boundary condition in [O] specified at ∼100 km by NRLMSISE-00 does not match data in this region from SABER. The [O] from SABER (at 97–100 km) has larger densities at solstices and at summer mid-high latitudes, opposite to that of MSIS. It was found that [O] from WACCM-X at ∼100 km matches the data better and was then used as lower boundary condition in GITM. The seasonal and latitudinal variations of other parameters are similar between MSIS and WACCM-X in this altitude region. Using GITM driven by the opposite [O] distribution from WACCM-X (G/WX) corrects for the summer-winter gradient. However, it does not improve the SAO at higher altitudes, but rather leads to maxima around solstices, which is 180° out of phase with respect to the MSIS driven GITM (G/MSIS) and the T-I observations. This is especially interesting, since the pure WACCM-X model has the appropriate phase of the upper thermospheric SAO, when compared to data. Nudging the dynamics in GITM toward WACCM-X up to 140 km (G/NUDGE), reduces the amplitude of this oppositely phased SAO, but does not completely correct it.

We find that the maximum change in the SAO phase in GITM between the lower boundary and the upper thermosphere is ∼30 days, which is not enough to have a phase shift on a seasonal scale. We reveal that in G/WX and G/NUDGE simulations, the maxima in global mean [O] during the solstices are a result of the weaker thermospheric spoon mixing in GITM as compared to WACCM-X. Larger [O] at summer high latitudes in the MLT lead to accumulation of [O] at lower latitudes in the thermosphere during solstices, which further increases the amplitude of the oppositely phased SAO. G/MSIS is able to achieve the right phase of T-I SAO because it starts with the equinoctial maxima in [O] at the lower boundary. For G/NUDGE, equatorward winds and the resulting convergence between 100 and 140 km also add to this accumulation of [O]. The pure WACCM-X model also has the wrong phase of the SAO in the lower thermosphere, as it transitions from solstitial maxima toward equinoctial maxima between the altitudes ranging from 100 to 200 km. Since, several studies have shown that the global mean [O] and O/N_2 in the lower thermosphere have equinoctial maxima, we suggest that the phase transition from solstitial to equinoctial maxima in the global mean SAO should occur in the altitude region of ∼100–140 km.

Since the [O] distribution in WACCM-X matches SABER observations at 97–100 km, there should be additional mechanisms acting in the lower thermosphere that decrease solstitial densities and nudge the phase of SAO toward equinoctial maxima. These could include stronger thermospheric spoon circulation, stronger lower thermospheric residual circulation during solstices, and a seasonal variation in K_{zz}. It is also possible that sub-grid processes such as gravity wave breaking could act as a momentum source for the meridional winds, enhancing the meridional transport during the solstices. The exact mechanisms that drive the phase transition of the SAO in the lower thermosphere are currently unknown and will be the subject of future studies.

Our results emphasize the importance of accurate representation of the MLT state and dynamics in the lower thermosphere in T-I models for better modeling of T-I SAO, and thus agree with the appraisal by Picone et al. (2013). We infer that the lower thermospheric region between 100 and 150 km is a complex and important region, as this is where the effect of the larger scale neutral dynamics is strongest. Finally, as new models and data sets are introduced, it becomes crucial to validate them with the older models and data sets; this can help in addressing the gaps in our knowledge of the physical mechanisms in the T-I region.

Data Availability Statement

GITM Simulations used in this study are available at https://doi.org/10.7302/9gp8-kx76. The atomic oxygen used in this study is from SABER data Version 2.0 and was downloaded from http://saber.gats-inc.com/data.php. The level 3 O/N_2 GUVI data were downloaded from http://guvitimed.jhuapl.edu/. Level 3 vector data from TIDI were downloaded from http://download.hao.ucar.edu/archive/tidi/data/vec0307a/. GNSS data can be accessed through the Madrigal distributed data system, http://millstonehill.haystack.mit.edu/, as provided to the community by the Massachusetts Institute of Technology under support from US National Science Foundation grant AGS-1952737. CHAMP and GRACE data were downloaded from http://thermosphere.tudelft.nl/.

Acknowledgments
This work was supported by NASA grant #80NSSC20K1581. McArthur Jones Jr. gratefully acknowledges support from NASA Heliophysics Early Career Investigator (NNH18ZDA001N-ECIP/18-ECIP_2–0018) and Theory, Modeling, and Simulations (19-HTMS19_2–0056) Programs. High computing resources were provided through Pleiades supercomputer by NASA Advanced Supercomputing (NAS) housed at NASA Ames Research Center and through Cheyenne supercomputer (doi:10.5065/D6RX99HX) by NCAR's Computational and Information Systems Laboratory sponsored by the National Science Foundation and other agencies.

References

Bartels, J. (1932). Terrestrial-magnetic activity and its relations to solar phenomena. *Terrestrial Magnetism and Atmospheric Electricity*, *37*(1), 1–52. https://doi.org/10.1029/te037i001p00001

Boller, B. R., & Stolov, H. L. (1970). Kelvin-helmholtz instability and the semiannual variation of geomagnetic activity. *Journal of Geophysical Research*, *75*(31), 6073–6084. https://doi.org/10.1029/ja075i031p06073

Brasseur, G., & Solomon, S. (1984). *Aeronomy of the middle atmosphere*. D. Reidel.

Bruinsma, S., Tamagnan, D., & Biancale, R. (2004). Atmospheric densities derived from champ/star accelerometer observations. *Planetary and Space Science*, *52*(4), 297–312. https://doi.org/10.1016/j.pss.2003.11.004

Bruinsma, S. L., & Forbes, J. M. (2008). Medium- to large-scale density variability as observed by CHAMP. *Space Weather*, *6*(8). https://doi.org/10.1029/2008sw000411

Burns, A. G., Solomon, S. C., Wang, W., Qian, L., Zhang, Y., Paxton, L. J., et al. (2015). Explaining solar cycle effects on composition as it relates to the winter anomaly. *Journal of Geophysical Research: Space Physics*, *120*(7), 5890–5898. https://doi.org/10.1002/2015ja021220

Burrage, M. D., Vincent, R. A., Mayr, H. G., Skinner, W. R., Arnold, N. F., & Hays, P. B. (1996). Long-term variability in the equatorial middle atmosphere zonal wind. *Journal of Geophysical Research*, *101*(D8), 12847–12854. https://doi.org/10.1029/96jd00575

Cageao, R., & Kerr, R. (1984). Global distribution of helium in the upper atmosphere during solar minimum. *Planetary and Space Science*, *32*(12), 1523–1529. https://doi.org/10.1016/0032-0633(84)90019-9

Chamberlin, P. C., Woods, T. N., & Eparvier, F. G. (2008). Flare irradiance spectral model (FISM): Flare component algorithms and results. *Space Weather*, *6*(5). https://doi.org/10.1029/2007sw000372

Christensen, A. B., Paxton, L. J., Avery, S., Craven, J., Crowley, G., Humm, D. C., & Zhang, Y. (2003). Initial observations with the Global Ultraviolet Imager (GUVI) in the NASA TIMED satellite mission. *Journal of Geophysical Research*, *108*(A12), 1451. https://doi.org/10.1029/2003ja009918

Cook, G. (1967). The large semi-annual variation in exospheric density: A possible explanation. *Planetary and Space Science*, *15*(4), 627–632. https://doi.org/10.1016/0032-0633(67)90036-0

Cook, G., & Scott, D. W. (1966). Exospheric densities near solar minimum derived from the orbit of echo 2. *Planetary and Space Science*, *14*(11), 1149–1165. https://doi.org/10.1016/0032-0633(66)90029-8

Cook, G. E. (1969a). Semi-annual variation in density at a height of 90 km. *Nature*, *222*, 969–971. https://doi.org/10.1038/222969a010.1038/222969a0

Cook, G. E. (1969b). The semi-annual variation in the upper atmosphere: A review. *Annales de Geophysique*, *25*, 451–469.

Dhadly, M. S., Emmert, J. T., Jones, M., Doornbos, E., Zawdie, K. A., Drob, D. P., & Conde, M. G. (2020). Oscillations in neutral winds observed by GOCE. *Geophysical Research Letters*, *47*, e2020GL089339. https://doi.org/10.1029/2020GL089339

Drob, D. P., Emmert, J. T., Meriwether, J. W., Makela, J. J., Doornbos, E., Conde, M., et al. (2015). An update to the horizontal wind model (HWM): The quiet time thermosphere. *Earth and Space Science*, *2*(7), 301–319. https://doi.org/10.1002/2014ea000089

Dunker, T., Hoppe, U.-P., Feng, W., Plane, J. M., & Marsh, D. R. (2015). Mesospheric temperatures and sodium properties measured with the alomar na lidar compared with WACCM. *Journal of Atmospheric and Solar-Terrestrial Physics*, *127*, 111–119. (Layered Phenomena in the Mesopause Region). https://doi.org/10.1016/j.jastp.2015.01.003

Emmert, J. T. (2009). A long-term data set of globally averaged thermospheric total mass density. *Journal of Geophysical Research*, *114*(A6), A06315. https://doi.org/10.1029/2009ja014102

Emmert, J. T. (2015a). Thermospheric mass density: A review. *Advances in Space Research*, *56*(5), 773–824. https://doi.org/10.1016/j.asr.2015.05.038

Emmert, J. T. (2015b). Altitude and solar activity dependence of 1967–2005 thermospheric density trends derived from orbital drag. *Journal of Geophysical Research: Space Physics*, *120*(4), 2940–2950. https://doi.org/10.1002/2015ja021047

Emmert, J. T., Drob, D. P., Picone, J. M., Siskind, D. E., Jones, M., Mlynczak, M. G., & Yuan, T. (2020). NRLMSIS 2.0: A whole-atmosphere empirical model of temperature and neutral species densities. *Earth and Space Science*, *8*, e2020EA001321. https://doi.org/10.1029/2020EA001321

Emmert, J. T., McDonald, S. E., Drob, D. P., Meier, R. R., Lean, J. L., & Picone, J. M. (2014). Attribution of interminima changes in the global thermosphere and ionosphere. *Journal of Geophysical Research: Space Physics*, *119*(8), 6657–6688. https://doi.org/10.1002/2013ja019484

Emmert, J. T., Picone, J. M., & Meier, R. R. (2008). Thermospheric global average density trends, 1967–2007, derived from orbits of 5000 near-earth objects. *Geophysical Research Letters*, *35*(5), L05101. https://doi.org/10.1029/2007gl032809

Forbes, J. M., Bruinsma, S. L., Zhang, X., & Oberheide, J. (2009). Surface-exosphere coupling due to thermal tides. *Geophysical Research Letters*, *36*(15), L15812. https://doi.org/10.1029/2009gl038748

Fuller-Rowell, T., Rees, D., Quegan, S., Moffett, R., Codrescu, M., & Millward, G. (1996). *A coupled thermosphere-ionosphere model (CTIM)* (p. 239). STEP Report.

Fuller-Rowell, T. J. (1998). The thermospheric spoonÄù: A mechanism for the semiannual density variation. *Journal of Geophysical Research*, *103*(A3), 3951–3956. https://doi.org/10.1029/97ja03335

Fuller-Rowell, T. J., & Evans, D. S. (1987). Height-integrated Pedersen and Hall conductivity patterns inferred from the TIROS-NOAA satellite data. *Journal of Geophysical Research*, *92*(A7), 7606–7618. https://doi.org/10.1029/ja092ia07p07606

Garcia, R. R., Dunkerton, T. J., Lieberman, R. S., & Vincent, R. A. (1997). Climatology of the semiannual oscillation of the tropical middle atmosphere. *Journal of Geophysical Research*, *102*(D22), 26019–26032. https://doi.org/10.1029/97jd00207

Garcia, R. R., & Solomon, S. (1985). The effect of breaking gravity waves on the dynamics and chemical composition of the mesosphere and lower thermosphere. *Journal of Geophysical Research*, *90*(D2), 3850–3868. https://doi.org/10.1029/jd090id02p03850

Grossmann, K. U., Kaufmann, M., & Gerstner, E. (2000). A global measurement of lower thermosphere atomic oxygen densities. *Geophysical Research Letters*, *27*(9), 1387–1390. https://doi.org/10.1029/2000gl003761

Groves, G. (1972). Annual and semi-annual zonal wind components and corresponding temperature and density variations, 60–130 km. *Planetary and Space Science*, *20*(12), 2099–2112. https://doi.org/10.1016/0032-0633(72)90066-9

Hagan, M. E., Maute, A., & Roble, R. G. (2009). Tropospheric tidal effects on the middle and upper atmosphere. *Journal of Geophysical Research*, *114*(A1), A01302. https://doi.org/10.1029/2008ja013637

Hedin, A. E. (1983). A revised thermospheric model based on mass spectrometer and incoherent scatter data: MSIS-83. *Journal of Geophysical Research*, *88*(A12), 10170–10188. https://doi.org/10.1029/ja088ia12p10170

Hedin, A. E. (1987). MSIS-86 thermospheric model. *Journal of Geophysical Research*, *92*(A5), 4649–4662. https://doi.org/10.1029/ja092ia05p04649

Hedin, A. E. (1991). Extension of the MSIS thermosphere model into the middle and lower atmosphere. *Journal of Geophysical Research*, *96*(A2), 1159–1172. https://doi.org/10.1029/90ja02125

Hedin, A. E., Salah, J. E., Evans, J. V., Reber, C. A., Newton, G. P., Spencer, N. W., et al. (1977). A global thermospheric model based on mass spectrometer and incoherent scatter data MSIS, 1. N_2 density and temperature. *Journal of Geophysical Research*, *82*(16), 2139–2147. https://doi.org/10.1029/ja082i016p02139

Hodges, R. R. (1969). Eddy diffusion coefficients due to instabilities in internal gravity waves. *Journal of Geophysical Research*, *74*(16), 4087–4090. https://doi.org/10.1029/ja074i016p04087

Holton, J. R. (1983). The influence of gravity wave breaking on the general circulation of the middle atmosphere. *Journal of the Atmospheric Sciences*, *40*(10), 2497–2507. https://doi.org/10.1175/1520-0469(1983)040<2497:tiogwb>2.0.co;2

Huba, J. D., & Liu, H.-L. (2020). Global modeling of equatorial spread f with SAMI3/WACCM-X. *Geophysical Research Letters*, *47*(14), e2020GL088258. https://doi.org/10.1029/2020GL088258

Jacchia, L. G. (1965). Static diffusion models of the upper atmosphere with empirical temperature profiles. *Smithsonian Contributions to Astrophysics*, *8*, 215. https://doi.org/10.5479/si.00810231.8-9.213

Jacchia, L. G. (1970). *New static models of the thermosphere and exosphere with empirical temperature profiles* (p. 313). SAO Special Report.

Jacchia, L. G. (1971). *Revised static models of the thermosphere and exosphere with empirical temperature profiles* (p. 332). SAO Special Report.

Jacchia, L. G. (1977). *Thermospheric temperature, density, and composition: new models* (Vol. 375). SAO Special Report.

Jacchia, L. G., Slowey, J. H., & Campbell, I. (1969). A study of the semi-annual density variation in the upper atmosphere from 1958 to 1966, based on satellite drag analysis. *Planetary and Space Science*, *17*(1), 49–60. https://doi.org/10.1016/0032-0633(69)90122-6

Jones Jr., M., Drob, D. P., Siskind, D. E., McCormack, J. P., Maute, A., McDonald, S. E., & Dymond, K. F. (2018a). Evaluating different techniques for constraining lower atmospheric variability in an upper atmosphere general circulation model: A case study during the 2010 sudden stratospheric warming. *Journal of Advances in Modeling Earth Systems*, *10*(12), 3076–3102. https://doi.org/10.1029/2018ms001440

Jones Jr., M., Emmert, J. T., Drob, D. P., Picone, J. M., & Meier, R. R. (2018b). Origins of the thermosphere-ionosphere semiannual oscillation: Reformulating the thermospheric spoon mechanism. *Journal of Geophysical Research: Space Physics*, *123*(1), 931–954. https://doi.org/10.1002/2017ja024861

Jones Jr., M., Emmert, J. T., Drob, D. P., & Siskind, D. E. (2017). Middle atmosphere dynamical sources of the semiannual oscillation in the thermosphere and ionosphere. *Geophysical Research Letters*, *44*(1), 12–21. https://doi.org/10.1002/2016gl071741

Jones Jr., M., Forbes, J. M., & Hagan, M. E. (2014). Tidal-induced net transport effects on the oxygen distribution in the thermosphere. *Geophysical Research Letters*, *41*(14), 5272–5279. https://doi.org/10.1002/2014gl060698

Jones Jr., M., Sutton, E. K., Emmert, J. T., Siskind, D. E., & Drob, D. P. (2021). On the effects of mesospheric and lower thermospheric oxygen chemistry on the thermosphere and ionosphere semiannual oscillation. *Journal of Geophysical Research: Space Physics*, *126*, e2020JA028647. https://doi.org/10.1029/2020ja028647

King-Hele, D., & Kingston, J. (1968). Air density at heights near 190 km in 1966–67, from the orbit of Secor 6. *Planetary and Space Science*, *16*(5), 675–691. https://doi.org/10.1016/0032-0633(68)90106-2

King-Hele, D., & Walker, D. M. (1969). Revised profiles of air density at heights of 130–180 km, from the orbits of 1968-59a and b. *Planetary and Space Science*, *17*(12), 2027–2029. https://doi.org/10.1016/0032-0633(69)90141-x

King-Hele, D. G. (1966). Semi-annual variation in upper-atmosphere density. *Nature*, *210*(5040), 1032. https://doi.org/10.1038/2101032a010.1038/2101032a0

King-Hele, D. G. (1967). Upper atmosphere density in 1966–67: The dominance of a semi-annual variation at heights near 200 km. *Nature*, *216*(5118), 880. https://doi.org/10.1038/216880a0

Lei, J., Matsuo, T., Dou, X., Sutton, E., & Luan, X. (2012). Annual and semiannual variations of thermospheric density: EOF analysis of CHAMP and GRACE data. *Journal of Geophysical Research*, *117*(A1), A01310. https://doi.org/10.1029/2011ja017324

Lin, S.-J. (2004). A vertically Lagrangian finite-volume dynamical core for global models. *Monthly Weather Review*, *132*(10), 2293–2307. https://doi.org/10.1175/1520-0493(2004)132<2293:avlfdc>2.0.co;2

Lindzen, R. S. (1981). Turbulence and stress owing to gravity wave and tidal breakdown. *Journal of Geophysical Research*, *86*(C10), 9707–9714. https://doi.org/10.1029/jc086ic10p09707

Liu, H., Foster, B. T., Hagan, M. E., McInerney, J. M., Maute, A., Qian, L., & Oberheide, J. (2010). Thermosphere extension of the whole atmosphere community climate model. *Journal of Geophysical Research*, *115*(A12), A12302. https://doi.org/10.1029/2010ja015586

Liu, H.-L., Bardeen, C. G., Foster, B. T., Lauritzen, P., Liu, J., Lu, G., et al. (2018a). Development and validation of the whole atmosphere community climate model with thermosphere and ionosphere extension (WACCM-X 2.0). *Journal of Advances in Modeling Earth Systems*, *10*(2), 381–402. https://doi.org/10.1002/2017ms001232

Liu, J., Liu, H., Wang, W., Burns, A. G., Wu, Q., Gan, Q., et al. (2018b). First results from the ionospheric extension of Waccm-X during the deep solar minimum year of 2008. *Journal of Geophysical Research: Space Physics*, *123*(2), 1534–1553. https://doi.org/10.1002/2017ja025010

Liu, X., Wang, W., Thayer, J. P., Burns, A., Sutton, E., Solomon, S. C., et al. (2014). The winter helium bulge revisited. *Geophysical Research Letters*, *41*(19), 6603–6609. https://doi.org/10.1002/2014gl061471

Lühr, H., Rother, M., Khler, W., Ritter, P., & Grunwaldt, L. (2004). Thermospheric upwelling in the cusp region: Evidence from CHAMP observations. *Geophysical Research Letters*, *31*(6), L06805. https://doi.org/10.1029/2003gl019314

Malhotra, G., Ridley, A. J., Marsh, D. R., Wu, C., Paxton, L. J., & Mlynczak, M. G. (2020). Impacts of lower thermospheric atomic oxygen on thermospheric dynamics and composition using the global ionosphere thermosphere model. *Journal of Geophysical Research: Space Physics*, *125*(9), e2020JA027877. https://doi.org/10.1029/2020JA027877

Malhotra, G., Ruohoniemi, J. M., Baker, J. B. H., Hibbins, R. E., & McWilliams, K. A. (2016). Hf radar observations of a quasi-biennial oscillation in midlatitude mesospheric winds. *Journal of Geophysical Research: Atmospheres*, *121*(2112), 12677–12689. https://doi.org/10.1002/2016jd024935

Maute, A., Hagan, M. E., Yudin, V., Liu, H.-L., & Yizengaw, E. (2015). Causes of the longitudinal differences in the equatorial vertical e b drift during the 2013 SSW period as simulated by the time-gcm. *Journal of Geophysical Research: Space Physics*, *120*(6), 5117–5136. https://doi.org/10.1002/2015ja021126

Mayr, H. G., Harris, I., & Spencer, N. W. (1978). Some properties of upper atmosphere dynamics. *Reviews of Geophysics*, *16*(4), 539–565. https://doi.org/10.1029/rg016i004p00539

Mayr, H. G., & Volland, H. (1972). Theoretical model for the latitude dependence of the thermospheric annual and semiannual variations. *Journal of Geophysical Research*, *77*(34), 6774–6790. https://doi.org/10.1029/ja077i034p06774

McDonald, S. E., Sassi, F., & Mannucci, A. J. (2015). SAMI3/SD-WACCM-X simulations of ionospheric variability during northern winter 2009. *Space Weather*, *13*(9), 568–584. https://doi.org/10.1002/2015sw001223

McLandress, C., Shepherd, G. G., Solheim, B. H., Burrage, M. D., Hays, P. B., & Skinner, W. R. (1996). Combined mesosphere/thermosphere winds using WINDII and HRDI data from the upper atmosphere research satellite. *Journal of Geophysical Research*, *101*(D6), 10441–10453. https://doi.org/10.1029/95jd01706

Miyoshi, Y., Fujiwara, H., Jin, H., & Shinagawa, H. (2014). A global view of gravity waves in the thermosphere simulated by a general circulation model. *Journal of Geophysical Research: Space Physics*, *119*(7), 5807–5820. https://doi.org/10.1002/2014ja019848

Mlynczak, M. G. (1996). Energetics of the middle atmosphere: Theory and observation requirements. *Advances in Space Research*, *17*(11), 117–126. https://doi.org/10.1016/0273-1177(95)00739-2

Mlynczak, M. G. (1997). Energetics of the mesosphere and lower thermosphere and the SABER experiment. *Advances in Space Research*, *20*(6), 1177–1183. https://doi.org/10.1016/S0273-1177(97)00769-2

Mlynczak, M. G., Hunt, L. A., Mast, J. C., Thomas Marshall, B., Russell, J. M., Smith, A. K., et al. (2013). Atomic oxygen in the mesosphere and lower thermosphere derived from SABER: Algorithm theoretical basis and measurement uncertainty. *Journal of Geophysical Research: Atmospheres*, *118*(11), 5724–5735. https://doi.org/10.1002/jgrd.50401

Newell, R. E. (1966). Thermospheric energetics and a possible explanation of some observations of geomagnetic disturbances and radio aurorae. *Nature*, *211*, 700–703. https://doi.org/10.1038/211700a010.1038/211700a0

Paetzold, H. K., & Zschörner, H. (1961). An annual and a semiannual variation of the upper air density. *Geofisica Pura e Applicata*, *48*, 85–92. https://doi.org/10.1007/BF01992371

Panka, P. A., Kutepov, A. A., Rezac, L., Kalogerakis, K. S., Feofilov, A. G., Marsh, D., et al. (2018). Atomic oxygen retrieved from the saber 2.0- and 1.6-μm radiances using new first-principles nighttime OH(v) model. *Geophysical Research Letters*, *45*(11), 5798–5803. https://doi.org/10.1029/2018gl077677

Paxton, L. J., Christensen, A. B., Humm, D. C., Ogorzalek, B. S., Pardoe, C. T., Morrison, D., et al. (1999). Global Ultraviolet Imager (GUVI): Measuring composition and energy inputs for the NASA Thermosphere Ionosphere Mesosphere Energetics and Dynamics (TIMED) mission. In A. M. Larar (Ed.), *Optical spectroscopic techniques and instrumentation for atmospheric and space research III* (Vol. 3756, pp. 265–276). SPIE. https://doi.org/10.1117/12.36638010.1117/12.366380

Picone, J. M., Hedin, A. E., Drob, D. P., & Aikin, A. C. (2002). NRLMSISE-00 empirical model of the atmosphere: Statistical comparisons and scientific issues-SIA 15. *Journal of Geophysical Research*, *107*(A12), SIA15-1–SIA15-16. https://doi.org/10.1029/2002ja009430

Picone, J. M., Meier, R. R., & Emmert, J. T. (2013). Theoretical tools for studies of low-frequency thermospheric variability. *Journal of Geophysical Research: Space Physics*, *118*(9), 5853–5873. https://doi.org/10.1002/jgra.50472

Qian, L., Burns, A., & Yue, J. (2017). Evidence of the lower thermospheric winter-to-summer circulation from SABER CO_2 observations. *Geophysical Research Letters*, *44*(20), 10100–10107. https://doi.org/10.1002/2017gl075643

Qian, L., Burns, A. G., Solomon, S. C., & Wang, W. (2013). Annual/semiannual variation of the ionosphere. *Geophysical Research Letters*, *40*(10), 1928–1933. https://doi.org/10.1002/grl.50448

Qian, L., Burns, A. G., Solomon, S. S., Smith, A. K., McInerney, J. M., Hunt, L. A., et al. (2018). Temporal variability of atomic hydrogen from the mesopause to the upper thermosphere. *Journal of Geophysical Research: Space Physics*, *123*(1), 1006–1017. https://doi.org/10.1002/2017ja024998

Qian, L., Solomon, S. C., & Kane, T. J. (2009). Seasonal variation of thermospheric density and composition. *Journal of Geophysical Research*, *114*(A1), A01312. https://doi.org/10.1029/2008ja013643

Qian, L., & Yue, J. (2017). Impact of the lower thermospheric winter-to-summer residual circulation on thermospheric composition. *Geophysical Research Letters*, *44*(9), 3971–3979. https://doi.org/10.1002/2017gl073361

Reigber, C., Lühr, H., & Schwintzer, P. (2002). Champ mission status. *Advances in Space Research*, *30*(2), 129–134. https://doi.org/10.1016/s0273-1177(02)00276-4

Rezac, L., Jian, Y., Yue, J., Russell, J. M., Kutepov, A., Garcia, R., & Bernath, P. (2015). Validation of the global distribution of CO_2 volume mixing ratio in the mesosphere and lower thermosphere from SABER. *Journal of Geophysical Research: Atmospheres*, *120*(23), 12067–12081. https://doi.org/10.1002/2015jd023955

Richmond, A. D., Ridley, E. C., & Roble, R. G. (1992). A thermosphere/ionosphere general circulation model with coupled electrodynamics. *Geophysical Research Letters*, *19*(6), 601–604. https://doi.org/10.1029/92gl00401

Ridley, A., Deng, Y., & Tth, G. (2006). The global ionosphere thermosphere model. *Journal of Atmospheric and Solar-Terrestrial Physics*, *68*(8), 839–864. https://doi.org/10.1016/j.jastp.2006.01.008

Rienecker, M. M., Suarez, M. J., Gelaro, R., Todling, R., Bacmeister, J., Liu, E., et al. (2011). MERRA: NASA's modern-era retrospective analysis for research and applications. *Journal of Climate*, *24*(14), 3624–3648. https://doi.org/10.1175/JCLI-D-11-00015.1

Rishbeth, H. (2007). Thermospheric targets. *Eos. Transactions American Geophysical Union*, *88*(17), 189–193. https://doi.org/10.1029/2007eo170002

Rishbeth, H., & Mendillo, M. (2001). Patterns of F2-layer variability. *Journal of Atmospheric and Solar-Terrestrial Physics*, *63*(15), 1661–1680. https://doi.org/10.1016/s1364-6826(01)00036-0

Rishbeth, H., & Müller-Wodarg, I. C. F. (1999). Vertical circulation and thermospheric composition: A modelling study. *Annales Geophysicae*, *17*(6), 794–805. https://doi.org/10.1007/s00585-999-0794-x

Rishbeth, H., Sedgemore-Schulthess, K. J. F., & Ulich, T. (2000). Semiannual and annual variations in the height of the ionospheric F2-peak. *Annales Geophysicae*, *18*(3), 285–299. https://doi.org/10.1007/s00585-000-0285-6

Russell, C. T., & McPherron, R. L. (1973). Semiannual variation of geomagnetic activity. *Journal of Geophysical Research*, *78*(1), 92–108. https://doi.org/10.1029/ja078i001p00092

Russell, J., Mlynczak, M., Gordley, L., Tansock, J., & Esplin, R. (1999). Overview of the SABER experiment and preliminary calibration results. *Proceedings of SPIE-The International Society for Optical Engineering*, *3756*. https://doi.org/10.1117/12.366382

Russell, J. P., Lowe, R., & Ward, W. (2004). Atomic oxygen annual and semi-annual variations in the mesopause region for mid and equatorial latitudes. *Journal of Atmospheric and Solar-Terrestrial Physics*, *66*(6), 451–461. (Dynamics and Chemistry of the MLT Region-PSMOS 2002 International Symposium). https://doi.org/10.1016/j.jastp.2004.01.004

Salinas, C. C. J. H., Chang, L. C., Liang, M. C., Yue, J., Russell, J., & Mlynczak, M. (2016). Impacts of SABER CO_2 Äêbased eddy diffusion coefficients in the lower thermosphere on the ionosphere/thermosphere. *Journal of Geophysical Research: Space Physics*, *121*(12), https://doi.org/10.1002/2016ja023161

Sassi, F., Liu, H.-L., & Emmert, J. T. (2016). Traveling planetary-scale waves in the lower thermosphere: Effects on neutral density and composition during solar minimum conditions. *Journal of Geophysical Research: Space Physics*, *121*(2), 1780–1801. https://doi.org/10.1002/2015ja022082

Sheese, P. E., McDade, I. C., Gattinger, R. L., & Llewellyn, E. J. (2011). Atomic oxygen densities retrieved from Optical Spectrograph and Infrared Imaging System observations of O_2 A-band airglow emission in the mesosphere and lower thermosphere. *Journal of Geophysical Research*, *116*(D1), D01303. https://doi.org/10.1029/2010jd014640

Siskind, D. E., Drob, D. P., Dymond, K. F., & McCormack, J. P. (2014). Simulations of the effects of vertical transport on the thermosphere and ionosphere using two coupled models. *Journal of Geophysical Research: Space Physics*, *119*(2), 1172–1185. https://doi.org/10.1002/2013ja019116

Smith, A. K., Harvey, V. L., Mlynczak, M. G., Funke, B., Garca-Comas, M., Hervig, M., et al. (2013). Satellite observations of ozone in the upper mesosphere. *Journal of Geophysical Research: Atmospheres*, *118*(11), 5803–5821. https://doi.org/10.1002/jgrd.50445

Smith, A. K., Marsh, D. R., Mlynczak, M. G., & Mast, J. C. (2010). Temporal variations of atomic oxygen in the upper mesosphere from SABER. *Journal of Geophysical Research*, *115*(D18), D18309. https://doi.org/10.1029/2009jd013434

Strickland, D. J., Evans, J. S., & Paxton, L. J. (1995). Satellite remote sensing of thermospheric o/N2 and solar EUV: 1. Theory. *Journal of Geophysical Research*, *100*(A7), 12217–12226. https://doi.org/10.1029/95ja00574

Sutton, E. K. (2011). Accelerometer-derived atmospheric density from the CHAMP and GRACE satellites. *Tech. Memo., DTIC ADA537198, Air Force Res. Lab. Kirtland AFB, N. M.*. Retrieved from https://apps.dtic.mil/sti/pdfs/ADA537198.pdf

Sutton, E. K. (2016). Interhemispheric transport of light neutral species in the thermosphere. *Geophysical Research Letters*, *43*(2412), 12325–12332. https://doi.org/10.1002/2016gl071679

Swenson, G., Yee, Y., Vargas, F., & Liu, A. (2018). Vertical diffusion transport of atomic oxygen in the mesopause region consistent with chemical losses and continuity: Global mean and inter-annual variability. *Journal of Atmospheric and Solar-Terrestrial Physics*, *178*, 47–57. https://doi.org/10.1016/j.jastp.2018.05.014

Swenson, G. R., Salinas, C. C. J. H., Vargas, F., Zhu, Y., Kaufmann, M., Jones, M., et al. (2019). Determination of global mean eddy diffusive transport in the mesosphere and lower thermosphere from atomic oxygen and carbon dioxide climatologies. *Journal of Geophysical Research: Atmospheres*, *124*(23), 13519–13533. https://doi.org/10.1029/2019jd031329

Tapley, B. D., Bettadpur, S., Watkins, M., & Reigber, C. (2004). The gravity recovery and climate experiment: Mission overview and early results. *Geophysical Research Letters*, *31*(9), L09607. https://doi.org/10.1029/2004gl019920

Vierinen, J., Coster, A. J., Rideout, W. C., Erickson, P. J., & Norberg, J. (2016). Statistical framework for estimating GNSS bias. *Atmospheric Measurement Techniques*, *9*(3), 1303–1312. https://doi.org/10.5194/amt-9-1303-2016

Volland, H., Wulf-Mathies, C., & Priester, W. (1972). On the annual and semiannual variations of the thermospheric density. *Journal of Atmospheric and Terrestrial Physics*, *34*(6), 1053–1063. https://doi.org/10.1016/0021-9169(72)90094-3

Walterscheid, R. L. (1982). The semiannual oscillation in the thermosphere as a conduction mode. *Journal of Geophysical Research*, *87*(A12), 10527–10535. https://doi.org/10.1029/ja087ia12p10527

Wang, J. C., Chang, L. C., Yue, J., Wang, W., & Siskind, D. E. (2017). The quasi 2 day wave response in TIME-GCM nudged with NOGAPS-ALPHA. *Journal of Geophysical Research: Space Physics*, *122*(5), 5709–5732. https://doi.org/10.1002/2016ja023745

Weimer, D. R. (2005). Improved ionospheric electrodynamic models and application to calculating joule heating rates. *Journal of Geophysical Research*, *110*(A5), A05306. https://doi.org/10.1029/2004ja010884

Wu, Q., Schreiner, W. S., Ho, S.-P., Liu, H.-L., & Qian, L. (2017). Observations and simulations of eddy diffusion and tidal effects on the semiannual oscillation in the ionosphere. *Journal of Geophysical Research: Space Physics*, *122*(1010), 10502–10510. https://doi.org/10.1002/2017ja024341

Yee, J.H. (2003). TIMED mission science overview. *John Hopkins APL Technical Digest*, *24*(2), 136–141. Apr–Jun.

Yu, T., Ren, Z., Yu, Y., Yue, X., Zhou, X., & Wan, W. (2020). Comparison of reference heights of O/N_2 and $\sum O/N_2$ based on GUVI dayside limb measurement. *Space Weather*, *18*(1), e2019SW002391. https://doi.org/10.1029/2019sw002391

Yue, J., Jian, Y., Wang, W., Meier, R., Burns, A., Qian, L., & Mlynczak, M. (2019). Annual and semiannual oscillations of thermospheric composition in TIMED/GUVI limb measurements. *Journal of Geophysical Research: Space Physics*, *124*(4), 3067–3082. https://doi.org/10.1029/2019ja026544

Zhang, S. P., McLandress, C., & Shepherd, G. G. (2007). Satellite observations of mean winds and tides in the lower thermosphere: 2. Wind imaging interferometer monthly winds for 1992 and 1993. *Journal of Geophysical Research*, *112*(D21), D21105. https://doi.org/10.1029/2007jd008457